

**TECHNISCHE
UNIVERSITÄT
DRESDEN**



CBG

Max Planck Institute
of Molecular Cell Biology
and Genetics

Setting YOUNG's modulus in the Subcellular Element Model

Diplomarbeit
zur Erlangung des akademischen Grades
Diplom-Physiker

vorgelegt von

Christian Bläsche
geboren am 14.07.1987 in Sebnitz

MAX PLANCK Institut of Molecular
Cell Biology and Genetics
MOSAIC Group
2014

Eingereicht am 12.02.2014

1. Gutachter: Prof. Dr. Frank Jülicher
2. Gutachter: Dr. Ivo F. Sbalzarini

Kurzdarstellung

Mit der zunehmenden Leistungsfähigkeit von Computern, beziehungsweise von Computerclustern, steigt die Bedeutung von numerischen Modellsimulationen im Bereich biologischer Systeme, welche aufgrund ihrer hohen Komplexität besonders rechenaufwändig sind. Mit dem "Subcellular Element Model" (SEM) können Gewebe modelliert werden, die aus vielen Hundert Zellen bestehen, ohne dabei die elementare Eigenschaft der Diskretheit von Zellen sowie deren äußere Gestalt zu vernachlässigen. Grundlegende physikalische Eigenschaften wie Elastizität können bislang jedoch nur mit erheblichen Fehlern implementiert werden. In dieser Arbeit wird ein Ansatz beschrieben, der sich, anstatt vom kubischen Gitter auszugehen, vom Modell der dichten Kugelpackung ableitet, und mit dem sich das elastische Modul wesentlich genauer modellieren lässt. Dies stellt einen günstigen Ausgangspunkt für künftige Erweiterungen der SEM dar.

Abstract

With the increasing performance of computers and computer clusters, the importance of numerical modelling in the field of biological systems has increased drastically. These systems are usually simulated at huge computational cost, because of their complex structure across scales. With the "Subcellular Element Model" (SEM), one can model tissues consisting of several hundreds of cells, without neglecting elementary properties, such as the discreteness of cells as well as their shape. So far, underlying physical properties like elasticity can only be implemented within a considerable uncertainty. In this thesis, a new approach based on close-packed lattices is developed. It yields a much more precise value for the elastic modulus with respect to previous publications. The results provide a basis for future extensions of the SEM.

Contents

List of Figures	vii
List of Tables	xi
1 Introduction	1
2 Theory	5
2.1 Elastic modulus in SEM	5
2.2 Simple cubic approach	7
2.3 Close-packed approach	9
2.3.1 HCP in 2D with periodic boundary condition	10
2.3.2 FCC in 3D with periodic boundary conditions	13
2.3.3 HCP in 2D without boundaries	16
2.3.4 FCC in 3D without boundaries	20
2.4 Selecting a potential	25
2.4.1 Modified MORSE potential	26
2.4.2 Parabola potential	27
3 Numerics	31
3.1 Experiment and pseudocode	31
3.2 Solver	33
3.3 Parameters	34
3.4 Language	35
4 Results	37
4.1 Periodic HCP in 2D and potential comparison	37
4.2 Periodic FCC in 3D	41
4.3 Open HCP in 2D	45
4.4 Open FCC in 3D	48

5	Error discussion	51
5.1	Solver error: δE^{solv}	52
5.2	Fixed-angle approximation: δE^α	52
5.3	Linear elongation approximation: $\delta E^{\Delta h}$	53
5.4	Parabolic potential approximation: δE^{pot}	55
5.5	Weighting factor: δE^w	56
6	Summary	57
	Bibliography	61

List of Figures

1.0.1	An equilibrated SEM cell composed of $N = 256$ elements. The right hand side shows the positions of all subcellular elements, while the left hand side illustrates a cut-away view of what could be understood as the cell boundary: a potential isosurface containing all subcellular elements. Image taken from [New07].	2
1.0.2	Grown from repeated cell growth and division, this single cell became a large cluster of more than 1000 cells. Image taken from [New07].	3
2.1.1	Components of the stress tensor acting on a small volume element. For a single stress component σ_{ij} , the first index i indicates the direction in which the stress acts, and the second index j denotes the plane that the stress acts on.	6
2.2.1	Simple cubic configuration of Sub-cellular elements with $N_x = N_y = N_z = 5$. The box represents the cell containing $N = N_x N_y N_z$ elements. The force F splits up in $N_x N_y$ times f^* , each acts on one top element (red arrow).	8
2.3.1	Hexagonal close-packed arrangement of elements in 2D under stress, with periodic boundary in x-direction. The box represents the computational domain containing $N = N_x N_y$ elements, ghosts are marked half opaque. Here $N_x = 5$ and $N_y = 6$	10
2.3.2	One equilateral triangle of a hcp structure. The original position of the top element without applied force is indicated with half opacity.	11
2.3.3	Face-centered-cubic arrangement of elements in 3D under stress with periodic boundaries in x- and y-direction. The box represents the computational domain containing $N = 4N_x N_y N_z$ elements, ghosts are marked half opaque. Here $N_x = N_y = N_z = 2$	14
2.3.4	One equilateral pyramid of a fcc structure. The original position of the top element without applied force is indicated with half opacity.	14

2.3.5 Hexagonally-close-packed arrangement of elements in 2D under stress without boundaries. The box represents the cell containing $N = N_x N_y - \frac{N_y}{2}$ elements. Here $N_x = 5$ and $N_y = 6$	17
2.3.6 One deformed equilateral triangle of a hcp structure. The original positions without applied force are indicated with half opacity. In the upper left corner it is illustrated how f splits up.	17
2.3.7 Face-centered cubic arrangement of elements in 3D under stress without boundaries. The box represents the cell containing $N = N_x N_y N_z + (N_x - 1)(N_y - 1)N_z$ elements. Here $N_x = N_y = 4$ and $N_z = 3$	21
2.3.8 One deformed equilateral pyramid of an fcc structure. The original positions without applied force are indicated with half opacity. In the upper left corner it is illustrated how f splits up.	21
2.3.9 One layer of equilateral pyramids, where elements at the top are coloured red and at the bottom white. Here $N_x = 5, N_y = 4$ and $N_z = 1$. All nearest neighbour interactions are marked in different colors. A dashed line indicates an interaction which is neglected and solid lines are taken into account.	23
2.4.1 Scaled modified MORSE potential $V(r)/u_0$ in (a) on the left and associated force $F(r)r_{eq}/u_0$ in (b) on the right. Solid lines refer to $\rho = 2$ and dashed lines to $\rho = 4$. The black dots in (b) mark the inflection points of the potential $V(r)$. The tangents show the linear approximation at equilibrium.	27
2.4.2 Scaled parabola potential $V(r)/\kappa$ in (a) on the left and associated force $F(r)/\kappa$ in (b) on the right. To show the different ranges depending on the dimension of space, 2D is illustrated with a solid line and dashed lines represent 3D. Notice that dashed lines are partly covered.	28
4.1.1 $E_{OUT}(N_x)$ graph of the periodic HCP in 2D. N_y is set to 6 and all other parameters have their standard value. Time steps are of size 3.33×10^{-3} . Black crosses belong to the parabola V_P and blue ($\rho = 2$) and dark yellow ($\rho = 4$) crosses to the modified MORSE potential V_M	38
4.1.2 $E_{OUT}(N_y)$ graph in (a) and $ E_{OUT} - E_{OUT}(N_y = 2) (N_y)$ graph in (b) of the periodic HCP in 2D. The legend is valid for both plots. $N_x = 1$ and all other parameters have their standard value.	39

4.1.3	$E_{OUT}(r_{eq})$ graph in (a) and $ E_{OUT} - E_{IN} (r_{eq})$ graph in (b) of the periodic HCP in 2D. The legend is valid for both plots. The system has the size $N_x = 1$ and $N_y = 2$. All other parameters have their standard value.	39
4.1.4	$E_{OUT}(f^*)$ graph in (a) and $ E_{OUT} - E_{IN} (f^*)$ graph in (b) of the periodic HCP in 2D. The legend is valid for both plots. The system has the size $N_x = 1$ and $N_y = 2$. All other parameters have their standard value. . .	40
4.1.5	The graph shows the relative error as a function of the modelled modulus E_{IN} in (a) and the absolute error in (b) of the periodic HCP in 2D. The legend is valid for both plots. The system has the size $N_x = 1$ and $N_y = 2$. All other parameters have their standard value.	41
4.2.1	$E_{OUT}(N_x)$ graph in (a) and $E_{OUT}(N_y)$ graph in (b) of the periodic FCC in 3D. In (a) $N_y = N_z = 3$. In (b) $N_x = 1$ and $N_z = 3$. All other parameters have their standard value.	42
4.2.2	$E_{OUT}(N_z)$ graph in (a) and $ E_{OUT} - E_{OUT}(N_z = 1) (N_z)$ graph in (b) of the periodic FCC in 3D. $N_x = N_y = 1$ and all other parameters have their standard value.	42
4.2.3	$E_{OUT}(r_{eq})$ graph in (a) and $ E_{OUT} - E_{IN} (r_{eq})$ graph in (b) of the periodic FCC in 3D. The system has the size $N_x = N_y = N_z = 1$. All other parameters have their standard value.	43
4.2.4	$E_{OUT}(f^*)$ graph in (a) and $ E_{OUT} - E_{IN} (f^*)$ graph in (b) of the periodic FCC in 3D. The legend is valid for both plots. The system has the size $N_x = N_y = N_z = 1$. All other parameters have their standard value. . .	44
4.2.5	The graph shows the relative error as a function of the modelled modulus E_{IN} in (a) and the absolute error in (b) of the periodic FCC in 3D. The system has the size $N_x = N_y = N_z = 1$. All other parameters have their standard value.	44
4.3.1	$E_{OUT}(N_x)$ graph for different values N_y in (a) and three special cases of N_x - and N_y -dependence of E_{OUT} in (b) of the open HCP in 2D. All other parameters have their standard value. For a better visualization data points are linked through coloured lines, but they do not have any physical or numerical meaning.	46
4.3.2	$E_{OUT}(r_{eq})$ graph of the open HCP in 2D. The system has the size $N_x = N_y = 10$. All other parameters have their standard value.	46
4.3.3	$E_{OUT}(f^*)$ graph in (a) and $ E_{OUT} - E_{IN} (f^*)$ graph in (b) of the open HCP in 2D. The legend is valid for both plots. The system has the size $N_x = N_y = 10$. All other parameters have their standard value.	47

4.3.4	The graph shows the relative error as a function of the modelled modulus E_{IN} in (a) and the absolute error in (b) of the open HCP in 2D. The system has the size $N_x = N_y = 10$. All other parameters have their standard value.	47
4.4.1	$E_{OUT}(N_x)$ graph for different values N_y while $N_z = 1$ in (a) and $E_{OUT}(N_z)$ graph in (b) of the open FCC in 3D. All other parameters have their standard value. For a better visualization data points are linked through coloured lines, but they do not have any physical or numerical meaning.	49
4.4.2	$E_{OUT}(r_{eq})$ graph of the open FCC in 3D. The system has the size $N_x = N_y = N_z = 6$. All other parameters have their standard value.	49
4.4.3	$E_{OUT}(f^*)$ graph of the open FCC in 3D. The system has the size $N_x = N_y = N_z = 6$. All other parameters have their standard value.	50
4.4.4	The graph shows the relative error as a function of the modelled modulus E_{IN} in (a) and the absolute error in (b) of the open FCC in 3D. The system has the size $N_x = N_y = N_z = 6$. All other parameters have their standard value.	50
5.2.1	The error arising from the fixed-angle approximation δE^α . Shown is the plot of Equation 5.2.3 for positive strain ϵ in black and in red for negative strain ϵ respectively.	53
5.3.1	The error arising from the Δh TAYLOR expansion $\delta E^{\Delta h}$. Shown is the plot of Equation 5.3.2 for positive ϵ in black and in red for negative ϵ respectively.	54
5.4.1	The error arising from the choice of the potential δE^{pot} . Shown is the plot of Equation 5.4.1 for $\rho = 2$ and $\rho = 4$ in the case of stretching ($\epsilon > 0$) and compressing ($\epsilon < 0$).	55

List of Tables

2.1.1 Glossary of frequently used symbols. 7

3.2.1 The numerical error arising from using the EULER solver depends on the time step size dt . r_f is the distance between two elements after reaching computational equilibrium. The theoretical value r_{eq} is set to 1. 34

3.3.1 Unless otherwise stated r_{eq} , f^* and E_{IN} will always be set to their standard value given in this table. 35

1 Introduction

There are numerous examples in the field of biology in which numerical modelling of tissues and multicellular structures are employed in order to better understand and interpret experimental data. The application of numerical models is versatile and ranges from collective dynamics of unicellular organisms (myxobacteria [IMW⁺01] and slime molds [MH01]) to dynamics within a multicellular organism (ascular tumor growth [Byr03, SBGZ99], tumor angiogenesis [Cha00], embryogenesis [PMO00, DKKO95] and cell sorting [DKM95, GG92]). Often biological systems of interest contain thousands to millions of cells which in general have different phenotypes. In these scenarios, a lot of information needs to be processed. Forced by the limitation in computational power, one has to make a number of simplifying assumptions. This can be realized by limiting either the number of cells or the properties of a single cell model, such as internal structure, shape, polarization or discreteness. Neglecting active processes reduces complexity as well. Compromises can be made differently, resulting in a variety of models for cell populations, ranging from coarse-grained cell-density models, where tissues are treated as continuous media (e.g. [KJJ⁺05]) to single cell models covering aspects like cytoskeleton dynamics via actin polymerization ([RJM05]).

In 2005, NEWMAN introduced an intermediate model, which takes the shape of cells into account, while keeping the computational cost for simulating one thousand cells in affordable boundaries. As pointed out in [New05] the possibility for cells to change their shape and orientation is an essential ingredient to simulate coherent dynamics of tissues. One can find examples where morphological changes on large scales during gastrulation are caused by cell intercalation, having its origin in the elongation along a specific axis of individual cells [WSJL07]. The model is based on cells, each consisting of a number of so-called subcellular elements – points in a two- or three-dimensional space. The smallest volume containing all subcellular elements of a cell can be understood as a single biological cell, as illustrated in Figure 1.0.1. Time evolution of this model is then determined by the dynamics of the subcellular elements. Their equations of motion are stochastic differential equations of LANGEVIN type [VK92]. We consider a Subcellular Element Model (SEM) of N cells with M elements per cell. An element of the cell

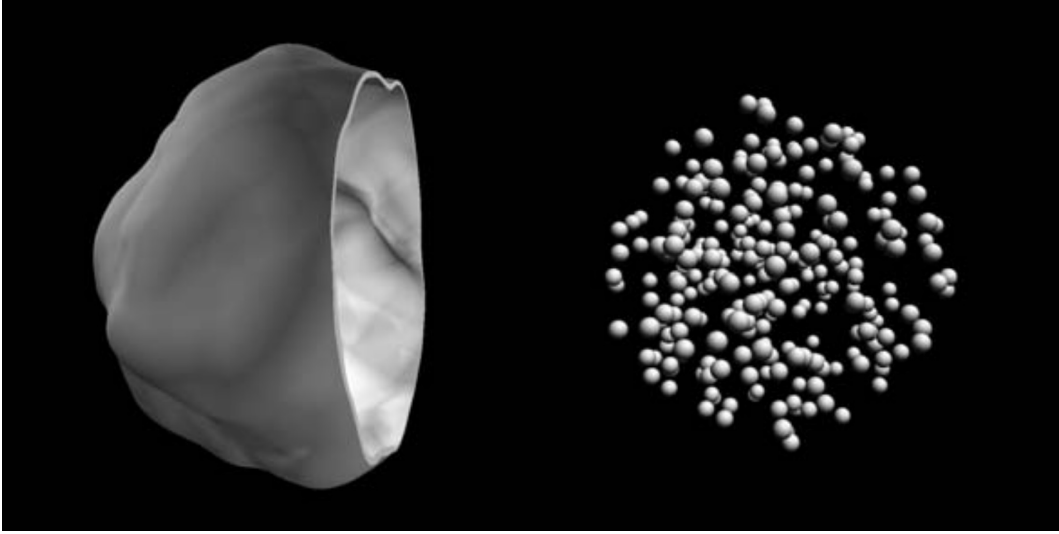


Figure 1.0.1: An equilibrated SEM cell composed of $N = 256$ elements. The right hand side shows the positions of all subcellular elements, while the left hand side illustrates a cut-away view of what could be understood as the cell boundary: a potential isosurface containing all subcellular elements. Image taken from [New07].

i is denoted by α_i and the position by \mathbf{x}_{α_i} , respectively. The reasonable assumption of over-damped element motion allows to neglect inertial effects and the equation of motion reads:

$$\eta \dot{\mathbf{x}}_{\alpha_i} = \xi_{\alpha_i} - \nabla_{\alpha_i} \sum_{\beta_i \neq \alpha_i} V_{intra}(|\mathbf{x}_{\alpha_i} - \mathbf{x}_{\beta_i}|) - \nabla_{\alpha_i} \sum_{j \neq i} \sum_{\beta_j} V_{inter}(|\mathbf{x}_{\alpha_i} - \mathbf{x}_{\beta_j}|). \quad (1.0.1)$$

The weak stochastic term ξ_{α_i} is GAUSSIAN noise, was introduced to model fluctuations in the cytoskeleton:

$$\langle \xi_{\alpha_i}^m(t) \xi_{\beta_j}^n(t') \rangle = 2D\eta^2 \delta_{i,j} \delta_{\alpha_i, \beta_j} \delta^{mn} \delta(t - t'), \quad (1.0.2)$$

where m and n are labels of vector components. The damping constant η scales the velocity and models viscous drag due to cytoplasm. On the right hand side of Equation 1.0.1, two interaction potentials appear: V_{intra} , a stronger potential to bind elements of the same cell together, and V_{inter} , which is weaker and lets surface elements of different cells adhere. These phenomenological potentials show the same characteristics, namely being repulsive at short distances, weakly attractive at intermediate distances, and roughly zero on large scales. We will introduce two possible potentials later in Section 2.4.

The SEM is a powerful tool and has a couple of advantages. It works without an un-

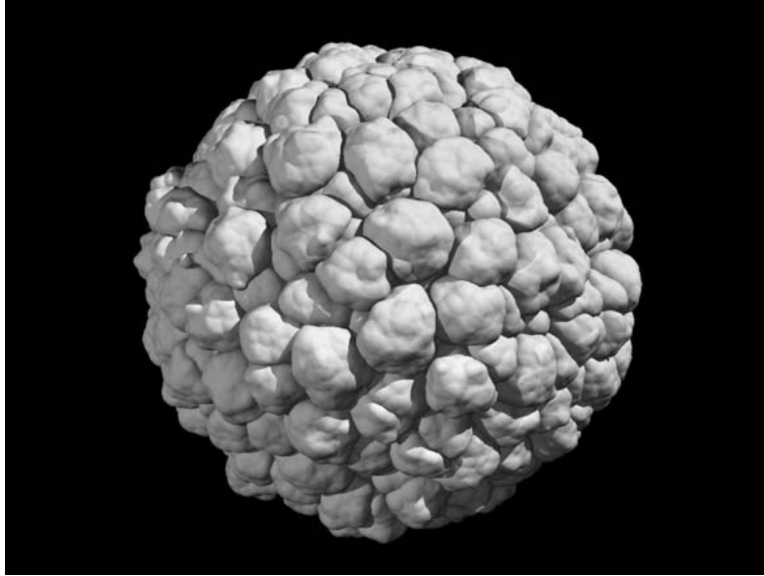


Figure 1.0.2: Grown from repeated cell growth and division, this single cell became a large cluster of more than 1000 cells. Image taken from [New07].

derlying lattice, thus avoiding the risk of causing strong artefacts [Gri05]. Cell growth and cell division as well as active processes can be implemented [SWN11, New07]. Figure 1.0.2 shows the result of a growth process, starting from a single cell.

Since subcellular elements have no real counterpart in nature, it is challenging to reproduce physical quantities. SANDERSIUS and NEWMAN have implemented the elastic modulus E in the SEM [SN08] and were able to retrieve values in the same order of magnitude as results obtained from measurements on living cells. When considering a model extension that includes active stress, it is necessary to ensure that basic properties, such as response under externally applied stress, is modelled correctly. The aim of this thesis is to reproduce the elastic modulus within the error of a few percent.

This thesis is structured as follows: In Chapter 2 we will start recapitulating the approach of SANDERSIUS and NEWMAN, and examine a new approach with different boundary conditions in two and three dimensions. We will derive four equations, which will then be tested numerically. Chapter 3 contains the explanation of the used program and the virtual experiment itself. Subsequently, we will focus on the computed results in Chapter 4. After an error discussion in Chapter 5, there will be the final Chapter 6, which will summarize this work and give an outlook.

2 Theory

After we briefly introduced the "Subcellular Element Model" (SEM) in the first chapter, the focus will be on elasticity and how this property is connected to the model. So far there is a considerable inaccuracy even in this very elementary physical behaviour. This shall be our motivation for a new attempt to implement elasticity in the SEM.

The first section of this chapter will cover a short derivation of the fundamental equation for the elastic modulus and a brief discussion about the problem we try to solve. In the following section, we will recapitulate the simple cubic approach of SANDERSIUS and NEWMAN [SN08]. The next part will contain a detailed derivation of how YOUNG's modulus can be implemented in the SEM when starting from close packing. Four scenarios with increasing complexity will be studied not only for didactic reasons, but also because of their relevance to biological systems. We will finish this chapter with a short discussion about the choice of the intercellular potentials.

2.1 Elastic modulus in SEM

Any physical theory of materials must predict the material's response to an applied mechanical force. When neglecting temperature, electromagnetic fields and inner structure, and restricting the problem to "small" forces (or stress), we can linearise the stress strain relation and write HOOKE's Law in its most general form for continuous media using EINSTEIN notation:

$$\sigma_{ij} = C_{ijkl}\epsilon_{kl}. \quad (2.1.1)$$

The stress σ_{ij} indicates the stress in i -direction acting on the j -plane of an infinitesimal material volume as illustrated in Figure 2.1.1. Strain of k -plane in l -direction is denoted by ϵ_{kl} . In three dimensions the 4th order tensor C has 81 entries and is called elastic tensor. In general there are maximal 21 independent components, since the stress and strain tensor as well as C are symmetric. To go on we need to apply the symmetry of isotropy to the elastic tensor, although cells of interest may be anisotropic. By doing this its 21 entries reduce to two independent quantities called YOUNG's or elastic

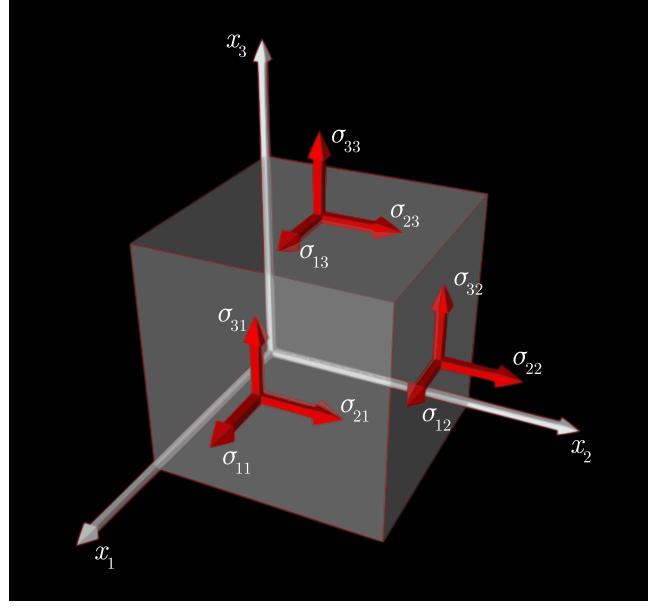


Figure 2.1.1: Components of the stress tensor acting on a small volume element. For a single stress component σ_{ij} , the first index i indicates the direction in which the stress acts, and the second index j denotes the plane that the stress acts on.

modulus E and POISSON'S ratio ν . The elastic modulus links stress and strain on one axis. POISSON'S ratio is a measure for the transverse to axial deformation. Using VOIGT notation, Equation 2.1.1 can be formed into $\underline{\epsilon} = \underline{C}^{-1}\underline{\sigma}$, where

$$C^{-1} = \begin{bmatrix} \frac{1}{E} & -\frac{\nu}{E} & -\frac{\nu}{E} & 0 & 0 & 0 \\ -\frac{\nu}{E} & \frac{1}{E} & -\frac{\nu}{E} & 0 & 0 & 0 \\ -\frac{\nu}{E} & -\frac{\nu}{E} & \frac{1}{E} & 0 & 0 & 0 \\ 0 & 0 & 0 & \frac{2(1+\nu)}{E} & 0 & 0 \\ 0 & 0 & 0 & 0 & \frac{2(1+\nu)}{E} & 0 \\ 0 & 0 & 0 & 0 & 0 & \frac{2(1+\nu)}{E} \end{bmatrix}.$$

POISSON'S ratio shall not be of interest in this thesis, since we want to focus on one-axis stress, thus the equation set collapses to the well-known scalar equation for YOUNG'S modulus [Rec90]:

$$E = \frac{\sigma}{\epsilon}. \quad (2.1.2)$$

The strain ϵ depends on the length with (l) and without applied force (l_0) such that $\epsilon = \frac{l-l_0}{l_0}$. For the stress σ , the relation $\sigma = \frac{F}{A}$ holds, where F symbolizes the force which acts on an Area A .

With element-element interaction potentials in SEM, stiffness can be modelled. Hence, we look for a proper potential or force field so that applying stress to the SEM cell results in the right strain according to Equation 2.1.2. We will apply stress to the modelled cell and measure the strain after elements have settled down. In general, after compressing or stretching, one deals with multiple coupled non-HOOKEean springs at equilibrium. But although we are faced with this static problem, there is still the need for introducing a cut-off radius or a potential in which next-nearest neighbour interactions can be neglected, otherwise it will be a very complex system. Non-linearity poses an additional problem, since the underlying constitutive equation, HOOKE's law, is only of linear order. For the following derivations, we will use HOOKE's law for springs to describe the interacting force, with κ being the spring constant and Δr the elongation¹.

$$f = \kappa \cdot \Delta r \quad (2.1.3)$$

N_x, N_y, N_z	Number of elements or primitive cells in x-,y- and z-direction
r_{eq}	Distance between two equilibrated elements
l_x, l_y, l_z	Spatial dimensions of the system
F	Applied force in total
f^*	Applied force on one element
f	Force between two elements
κ	Spring constant between two elements
Δr	Elongation between two elements ($r - r_{eq}$)
Δh	Elongation of between two layers of elements
Δl	Elongation in total

Table 2.1.1: Glossary of frequently used symbols.

2.2 Simple cubic approach

There is an approach to achieve a forcefield, where an elastic modulus can be inserted, done by SANDERSIUS and NEWMAN [SN08]. It is based on a simple cubic lattice of elements and contains a scaling law to get the elastic behaviour independent of the number of elements. Following this approach, we start in three dimensions (3D) with a simple cubic configuration (see Figure 2.2.1).

This may not be a stable equilibrium, but since we set the noise term² to zero, elements will stay in their positions. Only taking nearest neighbour interactions into

¹For a summary of the notation used in this work, see Table 2.1.1.

²See fundamental SEM equation 1.0.1 and 1.0.2.

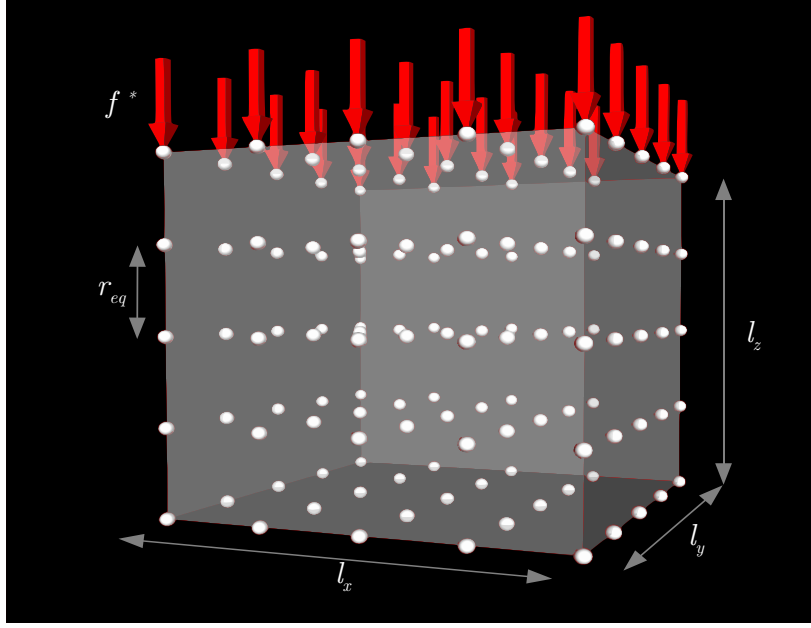


Figure 2.2.1: Simple cubic configuration of Sub-cellular elements with $N_x = N_y = N_z = 5$. The box represents the cell containing $N = N_x N_y N_z$ elements. The force F splits up in $N_x N_y$ times f^* , each acts on one top element (red arrow).

account, the elastic modulus for this system can be easily computed. The total number of elements N is given by $N = N_x N_y N_z$, and accordingly

$$l_x = r_{eq} (N_x - 1), \quad l_y = r_{eq} (N_y - 1), \quad l_z = r_{eq} (N_z - 1). \quad (2.2.1)$$

For the total force F , we sum up all forces f^* , where each acts on one element of the top surface³, so $F = N_x N_y f^*$. The stress can now be written as:

$$\sigma = \frac{F}{A} = \frac{N_x N_y f^*}{l_x l_y}. \quad (2.2.2)$$

After equilibration under stress, f^* acts on each subcellular element of the block. Interactions of neighbouring elements in an x-y plane are not affected by this force application, but those aligned in z-direction are, hence $f = f^*$. Furthermore, the elongation of the distance between two layers Δh equals the element interaction elongation Δr , because of its complete normal alignment to these layers. We rewrite Equation 2.1.2

³See red arrows in Figure 2.2.1

with $\epsilon = \frac{\Delta l_z}{l_z} = \frac{\Delta h}{r_{eq}}$:

$$\begin{aligned}
 E &= \frac{\sigma}{\epsilon} \\
 &= \frac{N_x N_y f^* r_{eq}}{l_x l_y \Delta h} \\
 &= \frac{N_x N_y}{(N_x - 1)(N_y - 1) r_{eq}} \underbrace{\frac{f}{\Delta r}}_{=\kappa}
 \end{aligned} \tag{2.2.3}$$

In this approach, E is a function of $\frac{f}{\Delta r}$. Thus, in order to obtain a constant elastic modulus, the force f has to be linear in Δr . Any non-linear forces result in a Δr -dependent elastic modulus. On the one hand, this could be a chance to model our tissue even in the difficult area of plasticity, but on the other hand, we will need other constitutive equations to define higher order terms. This possibility shall not be further considered here.

Following SANDERSIUS and NEWMAN, we consider a cube ($N_x = N_y = N_z = N^{\frac{1}{3}}$) and see that Equation 2.2.3 simplifies to

$$E = \frac{N^{\frac{2}{3}}}{N^{\frac{1}{3}} - 1} \frac{\kappa}{l}. \tag{2.2.4}$$

Knowing that a cell modelled by SEM will have a more amorphous structure, we approximate κ with the following scaling relation [SN08]

$$\kappa = \kappa_0 N^{-\frac{1}{3}} \left(1 - \lambda N^{-\frac{1}{3}}\right). \tag{2.2.5}$$

Where the scaling parameter $\lambda = 0.5$ gives an elastic modulus which is almost independent of N . As a consequence of implementing the scaling relation 2.2.5, E reduces to an approximation $E \approx \frac{\kappa_0}{l_0}$. In Section 4.1.1. of [SN08], there is an example where $\kappa_0 = 5 \times 10^{-3} \text{ N m}^{-1}$ and $l_0 = 10 \times 10^{-6} \text{ m}$, hence $E \approx 500 \text{ Pa}$. In contrast, the numerically measured elastic modulus was found to have a value of $357 \pm 4 \text{ Pa}$, where the error refers to different numbers of elements N .

To bridge this gap, we will try to formulate an alternative expression to Equation 2.2.3, in the form $\kappa = \kappa(E)$, by choosing a close-packed approach.

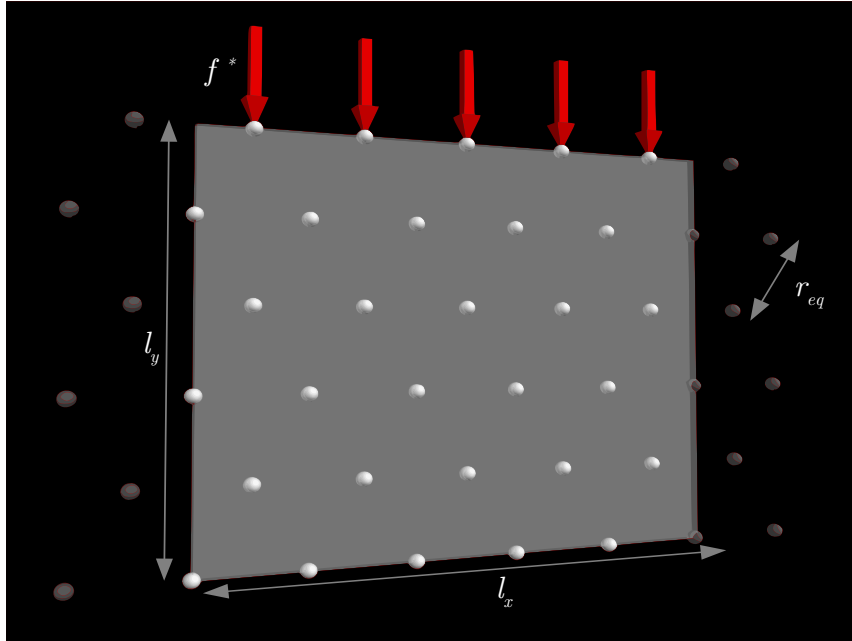


Figure 2.3.1: Hexagonal close-packed arrangement of elements in 2D under stress, with periodic boundary in x -direction. The box represents the computational domain containing $N = N_x N_y$ elements, ghosts are marked half opaque. Here $N_x = 5$ and $N_y = 6$.

2.3 Close-packed approach

The idea is to omit the introduction of a heuristic scaling law by simply starting the derivation for a different packing configuration. Staying closer to the "numerical reality", we may find more exact expressions than it was possible doing the simple cubic approach. If the noise term does not dominate the dynamics, elements will equilibrate at the energy minima of their potentials, near a close-packed configuration. Although the macroscopic shape of such an SEM cell may be a sphere, the core structure is best described by close packing. In order to understand the three dimensional system without boundaries, we will first have a look at hexagonal close-packed (hcp) elements in 2D with a periodic boundary condition in x -direction. In the next step, we will study a three-dimensional face-centered cubic (fcc) arrangement which also shall have periodic boundaries in x - and y -direction. Afterwards the focus will be on both systems with open boundaries.

2.3.1 HCP in 2D with periodic boundary condition

The starting point is a hcp system in 2D, as shown in Figure 2.3.1. For simplicity we want to start with a periodic boundary and therefore "ghost" elements are introduced.

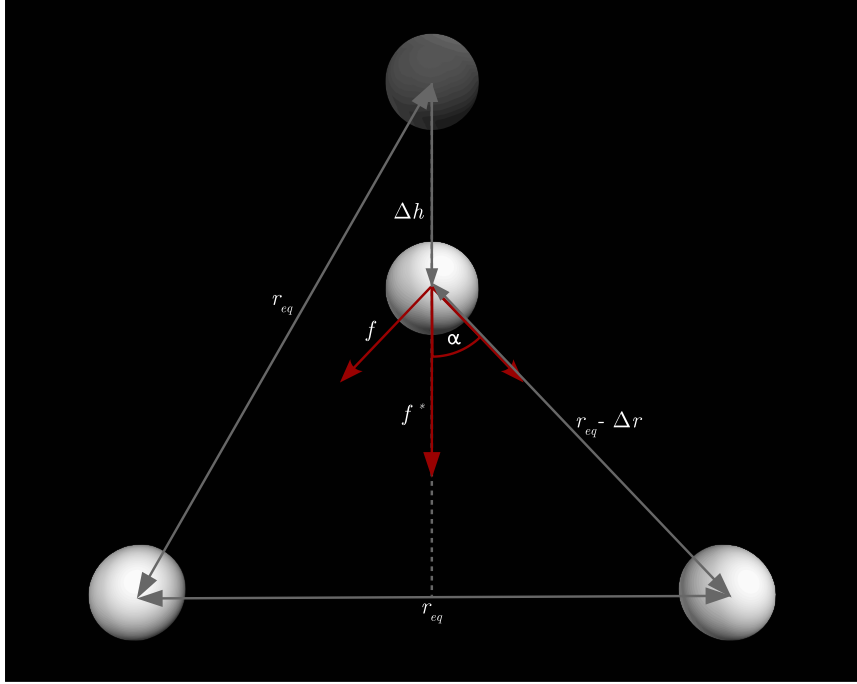


Figure 2.3.2: One equilateral triangle of a hcp structure. The original position of the top element without applied force is indicated with half opacity.

Those are copies outside the domain of elements which lie within the cutoff radius measured from the x -borders. Ghosts are marked half opaque. Thinking of a cylindrical surface periodicity is not only easier, it has relevance too. Taking Equation 2.1.2 one needs an expression for stress σ and strain ϵ dependent on element interactions, meaning $\sigma = \sigma(f)$ and $\epsilon = \epsilon(\Delta r)$.

In the 2D case we define stress by $\sigma = \frac{F}{l_x}$. Note that stress in 2D is not force per area, but force per length. The hcp structure consists of equilateral triangles and thus $l_x = N_x r_{eq}$. The total force F distributes equally to N_x elements at the top, $F = N_x f^*$. One has to remark that at equilibrium under stress, there is pressure everywhere in the domain, which leads to the fact that f^* is present at each element. Accordingly, it is sufficient to look at a single equilateral triangle as depicted in Figure 2.3.2. The force f^* separates into two element interaction forces f , $f^* = 2f \cos(\alpha)$. In general, the angle α between f and f^* has a f^* -dependency. We will keep that in mind, but not consider it in our calculation for the sake of simplicity. Thus, in the stressed case, we set $\alpha = 30^\circ$ as in the unstressed case. This turns out to be a good choice, since firstly it is a good approximation for small deformations and secondly it is somehow an average value for

pushing and pulling. As result we get:

$$\begin{aligned}\sigma &= \frac{F}{l_x} \\ &= \frac{f^*}{r_{eq}}\end{aligned}\tag{2.3.1}$$

$$\begin{aligned}&= \frac{2f \cos(30^\circ)}{r_{eq}} \\ &= \frac{\sqrt{3}f}{r_{eq}}\end{aligned}\tag{2.3.2}$$

Of course there is a force between elements of the same height acting in x -direction. In the open scenario we will name it f_2 with $f_2 = \sin(\alpha)f$. We started with a periodic boundary, because in this case f_2 has no effect. We find the reason for that in the limitation of the domain. Elements will finally be distributed equally over the whole width l_x , but this is also how they started. This results in no movement at all in x -direction. This is the reason why periodicity simplifies the problem.

Moving on to strain ϵ we look for terms of l_y and Δl_y . One easily finds l_y to be the sum of the height of $N_y - 1$ triangles illustrated in figure 2.3.1, leading to $l_y = (N_y - 1)r_{eq} \cos(30^\circ)$. In the same manner $\Delta l_y = (N_y - 1)\Delta h$. Since a linear force describes the element interaction, one needs ϵ as well as Δl_y and Δh to be linear in Δr . In Figure 2.3.2 we find a rectangular triangle for which PYTHAGORAS' theorem implies:

$$\begin{aligned}(r_{eq} - \Delta r)^2 &= \left(\frac{r_{eq}}{2}\right)^2 + \left(\frac{\sqrt{3}}{2}r_{eq} - \Delta h\right)^2 \text{ and} \\ \Delta h &= \frac{\sqrt{3}}{2}r_{eq} \pm \sqrt{(r_{eq} - \Delta r)^2 - \left(\frac{r_{eq}}{2}\right)^2}, \text{ respectively.}\end{aligned}\tag{2.3.3}$$

Knowing that $\Delta h(\Delta r = 0) = 0$ must be fulfilled, the "+"-solution is inappropriate. As a next step we perform a first order TAYLOR expansion of Equation 2.3.3 with respect to Δr at $\Delta r = 0$.

$$\begin{aligned}T_{\Delta h, \Delta r=0}^{(1)}(\Delta r) &= \frac{2}{\sqrt{3}}\Delta r \\ \Delta h &\approx \frac{2}{\sqrt{3}}\Delta r\end{aligned}\tag{2.3.4}$$

Plugging the latest results in the definition of ϵ one gets

$$\begin{aligned}
 \epsilon &= \frac{\Delta l_y}{l_y} \\
 &= \frac{(N_y - 1) \Delta h}{(N_y - 1) r_{eq} \cos(30^\circ)} \\
 &= \frac{\frac{2}{\sqrt{3}} \Delta r}{\frac{\sqrt{3}}{2} r_{eq}} \\
 &= \frac{4 \Delta r}{3 r_{eq}}.
 \end{aligned} \tag{2.3.5}$$

Using equation 2.3.2, 2.3.5 and $f = \kappa \Delta r$ we can write

$$\begin{aligned}
 E &= \frac{\sigma}{\epsilon} \\
 &= \frac{\sqrt{3} f 3 r_{eq}}{r_{eq} 4 \Delta r} \\
 &= \frac{3\sqrt{3}}{4} \kappa
 \end{aligned}$$

$$\boxed{\kappa(E) = \frac{4}{3\sqrt{3}} E} \tag{2.3.6}$$

This is a remarkable result since κ depends on nothing but E . Especially κ has no N_x -dependency, which is a reasonable fact since periodicity in x was assumed.

2.3.2 FCC in 3D with periodic boundary conditions

A similar expression can be derived for the face-centered cubic configuration as shown in Figure 2.3.3. As in the previous section the complexity is reduced by considering periodic boundaries. As an example we can think of a cell or a tissue in a tube or a sphere covered with a tissue of a certain thickness. We will perform the derivation of $\kappa(E)$ in the same manner as in Section 2.3.1.

The stress $\sigma = \frac{F}{A}$, where $A = l_x l_y$. With N_x and N_y one counts primitive fcc cells. They have a squared base with edge length $\sqrt{2} r_{eq}$, hence $A = 2 r_{eq}^2 N_x N_y$. The elementary geometry, which in 2D was the equilateral triangle, has now the shape of an equilateral pyramid illustrated in Figure 2.3.4. There are four of these pyramids in one primitive fcc cell. Since the size of its base is r_{eq}^2 , two lie next to each other and in addition we find one upside down pyramid on top of each which also fits into the same primitive

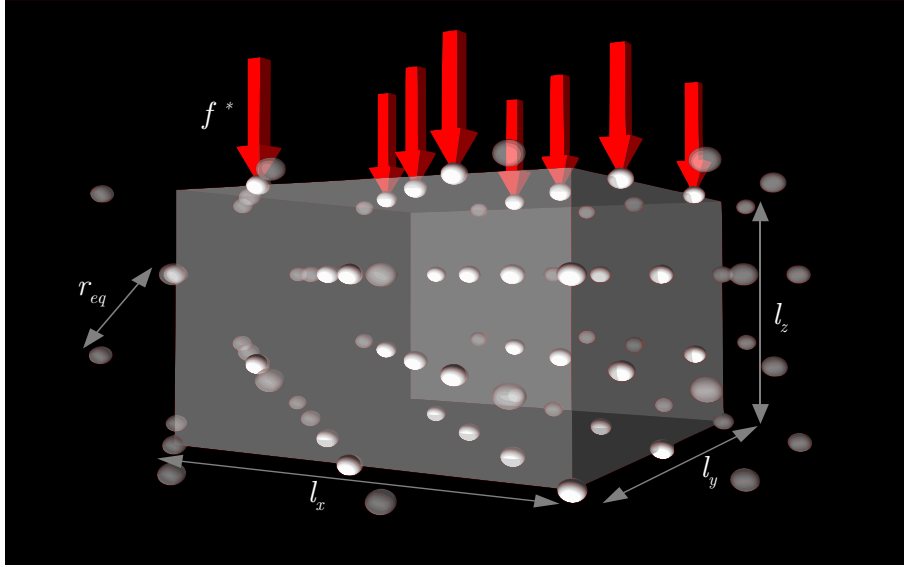


Figure 2.3.3: Face-centered-cubic arrangement of elements in 3D under stress with periodic boundaries in x- and y-direction. The box represents the computational domain containing $N = 4N_xN_yN_z$ elements, ghosts are marked half opaque. Here $N_x = N_y = N_z = 2$.

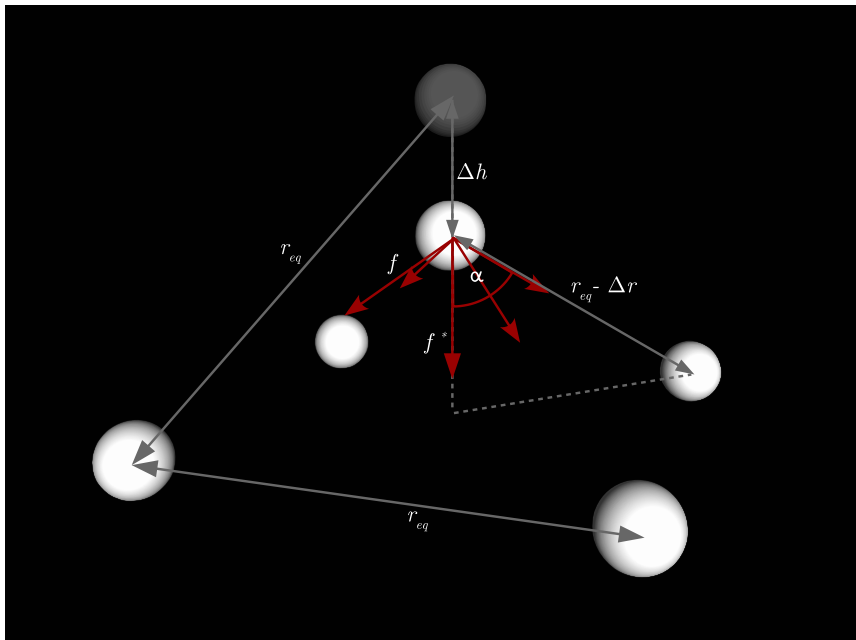


Figure 2.3.4: One equilateral pyramid of a fcc structure. The original position of the top element without applied force is indicated with half opacity.

cell. We need this geometry to understand how the total force F is distributed in the domain. At first, F separates onto all top particles which number is two per primitive cell, $F = 2N_x N_y f^*$. As discussed in the previous section, f^* is present in each layer. Secondly f^* splits up into $f^* = 4f \cos(\alpha)$, where we set $\alpha = 45^\circ$ and thereby disregard that α actually has a f^* -dependency. Again, there is no movement in x - and y -direction because of periodicity. We consider these assumption and write:

$$\begin{aligned}\sigma &= \frac{F}{A} \\ &= \frac{f^*}{r_{eq}^2}\end{aligned}\tag{2.3.7}$$

$$\begin{aligned}&= \frac{4f \cos(45^\circ)}{r_{eq}^2} \\ &= \frac{2\sqrt{2}f}{r_{eq}^2}\end{aligned}\tag{2.3.8}$$

Searching for the ϵ -expression we start with the height l_z . Since we took the bottom elements of the primitive fcc cell into full account we discard the top layer. In figure 2.3.3 $N_z = 2$ and one finds the top elements of the upper primitive cell missing. Therefore $l_z = (N_z - \frac{1}{2}) \sqrt{2}r_{eq}$. Because we have a stack of two pyramids per primitive cell, the axial elongation computes to $\Delta l_z = (N_z - \frac{1}{2}) 2\Delta h$. Also in this case we find a rectangular triangle, where PYTHAGORAS' theorem can be used to express Δh in terms of Δr (Figure 2.3.4). One has

$$\begin{aligned}(r_{eq} - \Delta r)^2 &= \left(\frac{r_{eq}}{\sqrt{2}}\right)^2 + \left(\frac{r_{eq}}{\sqrt{2}} - \Delta h\right)^2 \text{ and} \\ \Delta h &= \frac{r_{eq}}{\sqrt{2}} \pm \sqrt{(r_{eq} - \Delta r)^2 - \left(\frac{r_{eq}}{\sqrt{2}}\right)^2}, \text{ respectively.}\end{aligned}\tag{2.3.9}$$

A TAYLOR expansion of equation 2.3.9 ("-"-version) leads to the desired linear relation:

$$\Delta h \approx \sqrt{2}\Delta r.\tag{2.3.10}$$

For ϵ we write:

$$\begin{aligned}
 \epsilon &= \frac{\Delta l_z}{l_z} \\
 &= \frac{(N_z - \frac{1}{2}) 2\sqrt{2}\Delta r}{(N_z - \frac{1}{2}) \sqrt{2}r_{eq}} \\
 &= \frac{2\Delta r}{r_{eq}} \tag{2.3.11}
 \end{aligned}$$

Finally one can combine Equation 2.3.8, 2.3.11 and the element interaction force $f = \kappa\Delta r$:

$$\begin{aligned}
 E &= \frac{\sigma}{\epsilon} \\
 &= \frac{2\sqrt{2}f}{r_{eq}^2} \frac{r_{eq}}{2\Delta r} \\
 &= \frac{\sqrt{2}}{r_{eq}} \underbrace{f}_{=\kappa}
 \end{aligned}$$

$$\boxed{\kappa(E) = \frac{1}{\sqrt{2}}r_{eq}E} \tag{2.3.12}$$

Again $\kappa(E)$ does not depend on the number of elements, but linearly on r_{eq} .

2.3.3 HCP in 2D without boundaries

In most cases one is faced with biological systems that have no periodic boundary. So we go on with the open two-dimensional hcp structure shown in Figure 2.3.5. Compared to the previous scenario, the number of elements N is reduced by $\frac{N_y}{2}$ to get a symmetric shape.

Many expressions are very similar to those of Section 2.3.1. For example, the stress term is in fact equal so we can make use of Equation 2.3.2. But without boundaries, elements can move also sideways in x -direction. One has to take another force f_2 into account, which is orthogonal to f^* and spreads the lower elements of the equilateral triangle illustrated in Figure 2.3.6. PYTHAGORAS's theorem from above changes slightly

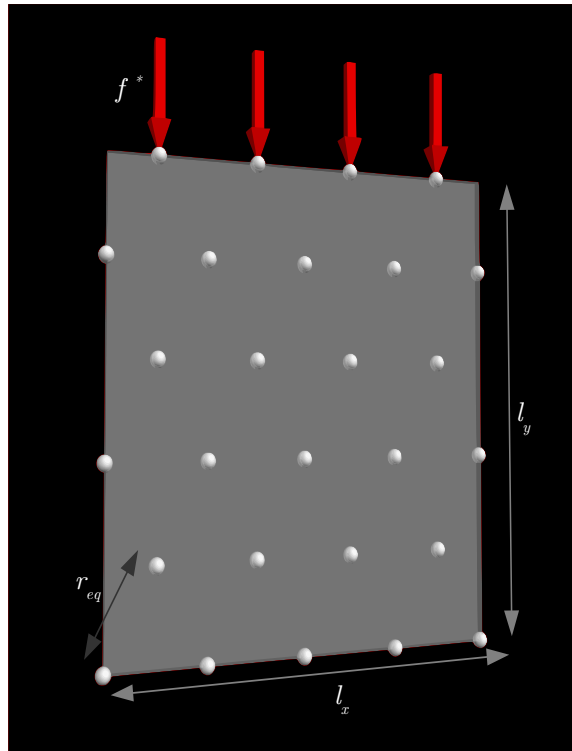


Figure 2.3.5: Hexagonally-close-packed arrangement of elements in 2D under stress without boundaries. The box represents the cell containing $N = N_x N_y - \frac{N_y}{2}$ elements. Here $N_x = 5$ and $N_y = 6$.

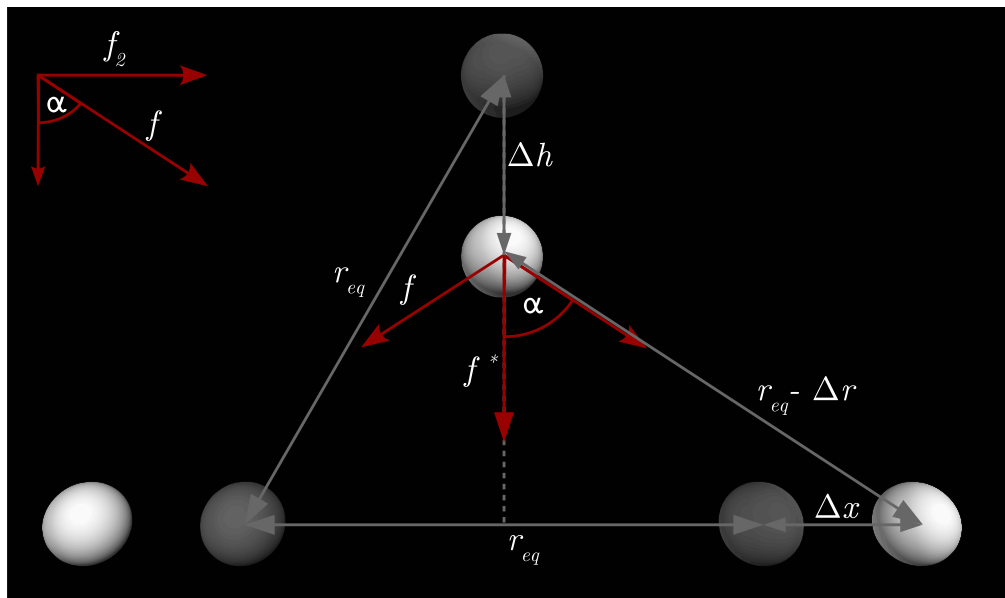


Figure 2.3.6: One deformed equilateral triangle of a hcp structure. The original positions without applied force are indicated with half opacity. In the upper left corner it is illustrated how f splits up.

to

$$(r_{eq} - \Delta r)^2 = \left(\frac{r_{eq}}{2} + \Delta x\right)^2 + \left(\frac{\sqrt{3}}{2}r_{eq} - \Delta h\right)^2 \quad \text{and}$$

$$\Delta h = \frac{\sqrt{3}}{2}r_{eq} \pm \sqrt{(r_{eq} - \Delta r)^2 - \left(\frac{r_{eq}}{2} + \Delta x\right)^2}, \quad \text{respectively.} \quad (2.3.13)$$

When linearising Equation 2.3.13 we have to decide for either Δr or Δx . Both are possible since there are two equations for κ : $f = \kappa\Delta r$ and $f_2 = \kappa 2\Delta x$. For conventional reasons we keep Δr and express Δx in terms of it. The elongation Δx turns out to be not constant and in all considered limits⁴ sufficient to have

$$\Delta x = w(N_x, N_y)\Delta r$$

with $w(N_x, N_y)$ being a weighting factor that depends on N_x and N_y . Starting with Figure 2.3.6 ($N_x = 2, N_y = 2$) one finds the relation between f and f_2 to be

$$f \underbrace{\sin(\alpha)}_{\approx \sin(30^\circ) = \frac{1}{2}} = f_2,$$

$$\kappa\Delta r \frac{1}{2} = \kappa 2\Delta x,$$

$$\Delta x = \frac{1}{4}\Delta r \quad \text{and}$$

$$w(2, 2) = \frac{1}{4}. \quad (2.3.14)$$

We let $N_x = 3$ and think of two such triangles next to each other. There appears another force acting between the two elements on the top. As a result these two are no longer on the symmetry axis of their triangle. f^* separates into two unequal forces thus making it complicated to find an analytical way to go on. A possible solution comes along as N_x goes to infinity. This limit will not converge to the value of the periodic scenario. The top element offset to their belonging symmetry axis gets smaller and smaller and we assume that f^* splits up as in Section 2.3.1 into $2\cos(\alpha)f$. The horizontal part of f does not only stretch the bottom elements, it also acts with the same strength between the top ones. Of course there is one interaction more at the bottom than at the top, but for simplicity we do not want to take that into account

⁴Considered limits are N_x and N_y being minimal, at the value of 2, and infinite large.

and rather write:

$$\begin{aligned}
f \underbrace{\sin(\alpha)}_{\approx \sin(30^\circ) = \frac{1}{2}} &= 2f_2, \\
\Delta r \frac{1}{2} &= 4\Delta x \text{ and} \\
w(\infty, 2) &= \frac{1}{8}.
\end{aligned} \tag{2.3.15}$$

The way the initial positions are set, we are just allowed to let N_y be even. This will let us have one f^* acting per equilateral triangle. An odd N_y will break the symmetry at the edges. If we want to make the system arbitrarily big, we are constrained to use even numbers for N_y .

Considering three triangles on top of each other ($N_x = 2, N_y = 4$) we notice that the upper triangles share one edge, hence two times f_2 contribute to Δx . Unfortunately this is not true for the lower triangle and so we are not able to calculate $w(2, 4)$. But in the limit of $N_y \rightarrow \infty$ we neglect the one at the bottom and get:

$$\begin{aligned}
f \underbrace{\sin(\alpha)}_{\approx \sin(30^\circ) = \frac{1}{2}} &= \frac{1}{2}f_2, \\
\Delta r \frac{1}{2} &= \Delta x \text{ and} \\
w(2, \infty) &= \frac{1}{2}.
\end{aligned} \tag{2.3.16}$$

In the limit of an infinite two-dimensional grid:

$$\begin{aligned}
f \underbrace{\sin(\alpha)}_{\approx \sin(30^\circ) = \frac{1}{2}} &= 2\frac{1}{2}f_2, \\
\Delta r \frac{1}{2} &= 2\Delta x \text{ and} \\
w(\infty, \infty) &= \frac{1}{4}.
\end{aligned} \tag{2.3.17}$$

For arbitrary sizes of N_x and N_y , we calculate the geometric mean and the weighting factor $w(N_x, N_y)$ computes to:

$$w(N_x, N_y) = \left[\frac{1}{4} \left(\frac{1}{8} \right)^{N_x-2} \left(\frac{1}{2} \right)^{N_y-2} \right]^{\frac{1}{N_x+N_y-3}} \tag{2.3.18}$$

With this result we can replace Δx in Equation 2.3.13 and linearise it with respect to Δr :

$$\Delta h = \frac{\sqrt{3}}{2}r_{eq} \pm \sqrt{(r_{eq} - \Delta r)^2 - \left(\frac{r_{eq}}{2} + w(N_x, N_y)\Delta r\right)^2} \text{ and}$$

$$\Delta h \approx T_{\Delta h, \Delta r=0}^{(1)}(\Delta r) = \frac{2 + w(N_x, N_y)}{\sqrt{3}}\Delta r. \quad (2.3.19)$$

The strain formula (2.3.5) changes to:

$$\epsilon = \frac{2(2 + w(N_x, N_y))}{3} \frac{\Delta r}{r_{eq}}. \quad (2.3.20)$$

Combining this result with the previously described stress term 2.3.2, we update the elastic modulus E and finally find the spring constant $\kappa(E)$:

$$E = \frac{3\sqrt{3}}{2(2 + w(N_x, N_y))} \frac{f}{\Delta r},$$

$$\kappa(E) = \frac{2}{3\sqrt{3}}(2 + w(N_x, N_y))E. \quad (2.3.21)$$

Unfortunately κ depends not only on E , but on N_x and N_y . This causes two problems for the numerical computation: Firstly κ is anisotropic and secondly changes with the shape of the cell. We will discuss this in Chapter 6.

2.3.4 FCC in 3D without boundaries

The last case to study shall be the closed packed arrangement without boundaries in three-dimensional space. Therefore we investigate the face-centered cubic system illustrated in Figure 2.3.7. With N_i ($i \in \{x, y, z\}$) we count equilateral pyramids instead of primitive fcc cells. In this way the derivation gets more intuitive, but there are slight changes compared to some expressions of Section 2.3.2.

Starting with the stress σ we find the area $A = (N_x - 1)(N_y - 1)r_{eq}^2$ and the total force $F = (N_x - 1)(N_y - 1)f^*$. The force on each pyramid f^* splits up as shown before and depicted in Figure 2.3.8. Hence the force f^* computes to $f^* = 4f \cos(45^\circ)$. One

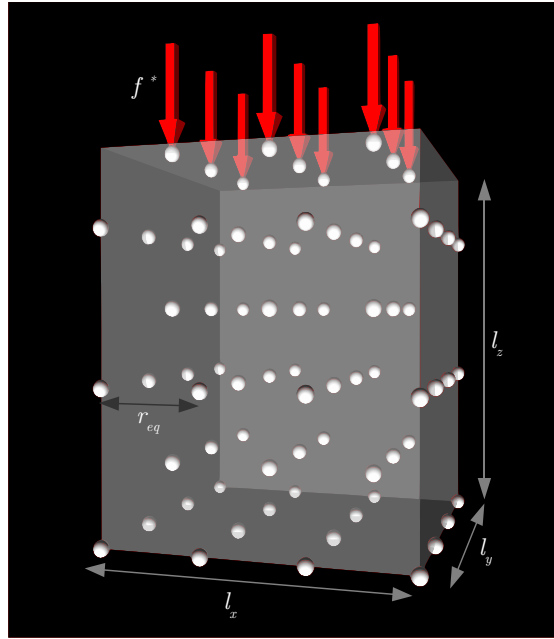


Figure 2.3.7: Face-centered cubic arrangement of elements in 3D under stress without boundaries. The box represents the cell containing $N = N_x N_y N_z + (N_x - 1)(N_y - 1)N_z$ elements. Here $N_x = N_y = 4$ and $N_z = 3$.

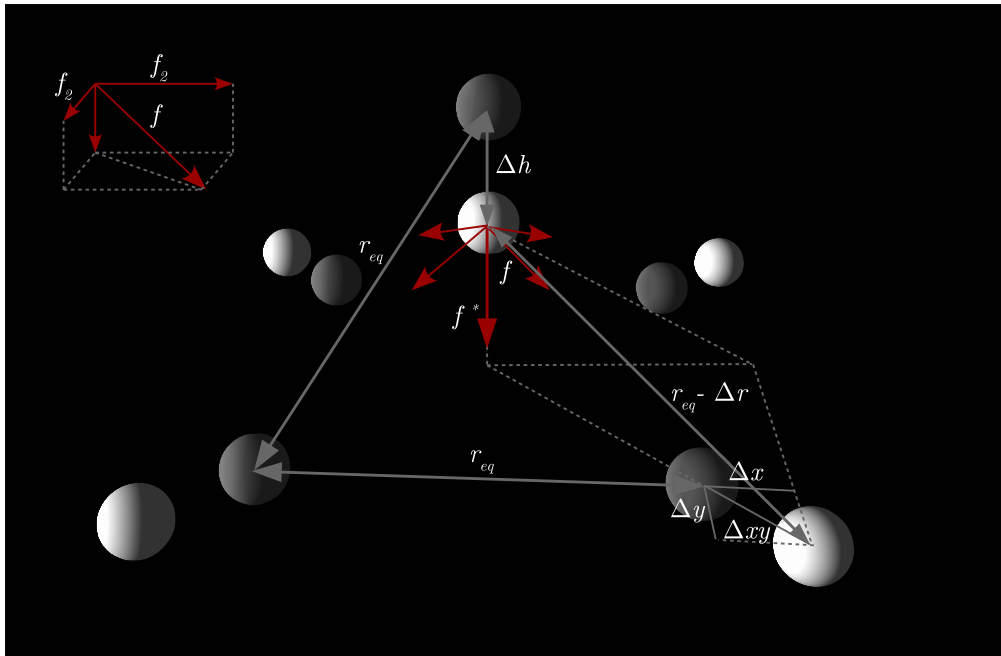


Figure 2.3.8: One deformed equilateral pyramid of an fcc structure. The original positions without applied force are indicated with half opacity. In the upper left corner it is illustrated how f splits up.

can calculate stress:

$$\begin{aligned}
\sigma &= \frac{F}{A} \\
&= \frac{(N_x - 1)(N_y - 1)4f \cos(45^\circ)}{(N_x - 1)(N_y - 1)r_{eq}^2} \\
&= \frac{2\sqrt{2}f}{r_{eq}^2} \tag{2.3.22}
\end{aligned}$$

We want to proceed with the more complicated problem of deriving a formula for the strain ϵ . The height computes to $l_z = (N_z - \frac{1}{2})\sqrt{2}r_{eq}$ and $\Delta l_z = (N_z - \frac{1}{2})2\Delta h$.

$$\begin{aligned}
\epsilon &= \frac{\Delta l_z}{l_z} \\
&= \frac{(N_z - \frac{1}{2})2\Delta h}{(N_z - \frac{1}{2})\sqrt{2}r_{eq}} \\
&= \frac{\sqrt{2}\Delta h}{r_{eq}} \tag{2.3.23}
\end{aligned}$$

One writes PYTHAGORAS' theorem for the triangle in Figure 2.3.8 which contains the top, one bottom element, and the center of the base. We obtain the elongation equation:

$$\begin{aligned}
(r_{eq} - \Delta r)^2 &= \left(\frac{r_{eq}}{\sqrt{2}} + \Delta xy\right)^2 + \left(\frac{r_{eq}}{\sqrt{2}} - \Delta h\right)^2 \text{ and} \\
\Delta h &= \frac{r_{eq}}{\sqrt{2}} \pm \sqrt{(r_{eq} - \Delta r)^2 - \left(\frac{r_{eq}}{\sqrt{2}} + \Delta xy\right)^2}, \text{ respectively.} \tag{2.3.24}
\end{aligned}$$

At this point one needs Δxy to be expressed in terms of Δr . We do this by again introducing the weighting factors $w(N_x, N_y, N_z)$ with $\Delta xy = w(N_x, N_y, N_z)\Delta r$. The weights can be derived from the force balance equation for f and f_2 . As a starting point $w(N_x, N_y, 1)$ shall be found with the help of Figure 2.3.9. What can be seen is one layer of equilateral pyramids. The force f^* acts on all red elements and each diagonal red line indicates the force f . Elements of the pyramids base are coloured white. The base elements are stretched by f_2 , the vertical and horizontal components of f . If lower elements are affected, f_2 is green, for upper ones f_2 is coloured in blue. From a numerical test run we find red elements on the edge to be quite flexible, so their interactions are only taken into account by the factor of 0.5 if the other involved element is not located at the edge. Neglected interactions are indicated with a dashed blue line. For deriving the force balance on the left hand side f_{left} , we simply sum

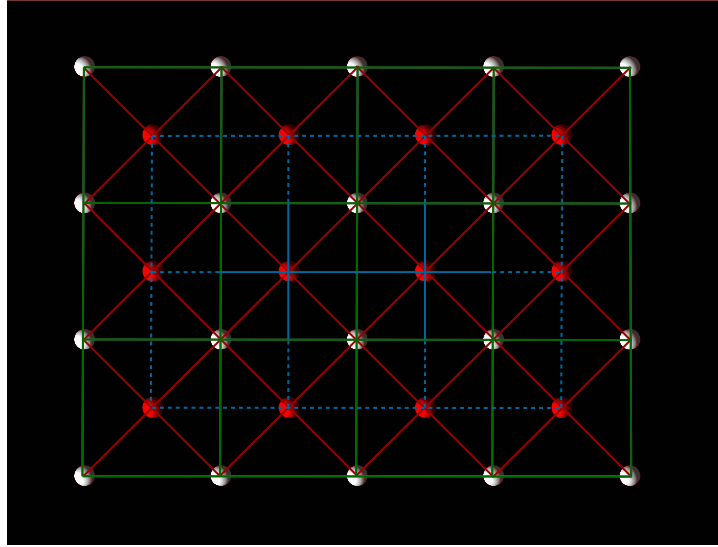


Figure 2.3.9: One layer of equilateral pyramids, where elements at the top are coloured red and at the bottom white. Here $N_x = 5, N_y = 4$ and $N_z = 1$. All nearest neighbour interactions are marked in different colors. A dashed line indicates an interaction which is neglected and solid lines are taken into account.

up the projections of f on the x- and y-axis and get $2 \sin(45^\circ) \sin(45^\circ) f$. But we also have to divide by two since two of these projected forces are involved in one element interaction at the bottom. Per pyramid one finds four times f , meaning all in all

$$f_{left} = 4 \sin^2(45^\circ) (N_x - 1) (N_y - 1) f. \quad (2.3.25)$$

The right hand side f_{right} consists of a sum of all interaction forces between elements of the same height. With a look at figure 2.3.9 we just have to count solid lines and easily we find $(N_x - 1)N_y + N_x(N_y - 1)$ green ones. The top elements on the edge have to be treated different since they move far too close to their red neighbours. As a good heuristic compromise we will count all four blue interactions of an inner top element but weight it with the factor $\frac{1}{2}$. For arrangements with $N_x > 2$ and $N_y > 2$ there are $\frac{1}{2} \cdot 4(N_x - 3)(N_y - 3)$ blue solid lines. Plugging this together gives us the amount of horizontal and vertical forces with the strength of f_2 which is the right hand side of the balance equation:

$$f_{right} = (2N_x N_y - N_x - N_y + 2(N_x - 3)(N_y - 3)) f_2. \quad (2.3.26)$$

The force balance reads as follows:

$$\begin{aligned}
 f_{left} &= f_{right} \\
 2(N_x - 1)(N_y - 1)f &= (2N_x N_y - N_x - N_y + 2(N_x - 3)(N_y - 3)) f_2 \\
 f_2 &= \frac{(N_x - 1)(N_y - 1)}{N_x N_y - \frac{1}{2}(N_x + N_y) + (N_x - 3)(N_y - 3)} f \quad (2.3.27)
 \end{aligned}$$

When writing HOOKE's law for f_2 , we remark that we assume symmetry and let $\Delta x = \Delta y$. For that reason we can always write $f_2 = \kappa 2\Delta x$. With $\Delta xy = \sqrt{2}\Delta x$ we can replace f_2 with $f_2 = \kappa\sqrt{2}\Delta xy$ in Equation 2.3.27. Furthermore we replace f by $\kappa\Delta r$ and the balance equation now reads

$$\kappa\sqrt{2}\Delta xy = \frac{(N_x - 1)(N_y - 1)}{N_x N_y - \frac{1}{2}(N_x + N_y) + (N_x - 3)(N_y - 3)} \kappa\Delta r.$$

If one compares the latest result with $\Delta xy = w(N_x, N_y, 1)\Delta r$ the expression for $w(N_x, N_y, 1)$ is found to be

$$w(N_x, N_y, 1) = \frac{1}{\sqrt{2}} \frac{(N_x - 1)(N_y - 1)}{N_x N_y - \frac{1}{2}(N_x + N_y) + (N_x - 3)(N_y - 3)}. \quad (2.3.28)$$

To achieve the $w(N_x, N_y, N_z)$ -formula we can apply the same strategy used for the derivation of Equation 2.3.15, where we built a stack out of triangles, saw that all but the lowest one share the base, formed the limit so we could neglect the singularity and finally built the geometric mean. In the three-dimensional case the pyramids share also their base with the one above or below, meaning that for the same elongation half of the force is needed. In the limit $N_z \rightarrow \infty$ this results in the weighting factor $w(N_x, N_y, \infty)$ being $2w(N_x, N_y, 1)$. Computing the N_z -dependent mean gives us:

$$w(N_x, N_y, N_z) = \left[w(N_x, N_y, 1) (2w(N_x, N_y, 1))^{N_z - 1} \right]^{\frac{1}{N_z}} \quad (2.3.29)$$

To have the elongation Δh (Equation 2.3.24) purely written in terms of $\Delta r, \Delta xy$ is to be replaced by $w(N_x, N_y, N_z)\Delta r$. We approximate Δh by performing a TAYLOR expansion with respect to Δr :

$$\Delta h \approx T_{\Delta h, \Delta r=0}^{(1)}(\Delta r) = \left(\sqrt{2} + w(N_x, N_y, N_z) \right) \Delta r.$$

Using this result, the former ϵ term from Equation 2.3.23 now reads:

$$\epsilon = \frac{\sqrt{2}}{r_{eq}} \left(\sqrt{2} + w(N_x, N_y, N_z) \right) \Delta r. \quad (2.3.30)$$

We write the elastic modulus $E = \frac{\sigma}{\epsilon}$ with the stress expressed in Equation 2.3.22 and ϵ from Equation 2.3.30 in the following form:

$$E = \frac{2\sqrt{2}}{r_{eq}^2} \frac{r_{eq}}{\sqrt{2} (\sqrt{2} + w(N_x, N_y, N_z))} \underbrace{\frac{f}{\Delta r}}_{=\kappa}$$

$$\boxed{\kappa = \left(1 + \frac{1}{\sqrt{2}} w(N_x, N_y, N_z) \right) r_{eq} E} \quad (2.3.31)$$

The problem of N_i -dependence ($i \in \{x, y, z\}$) is the same as in the previous section with Equation 2.3.21.

Finally, we have been able to derive formulas for κ in all scenarios with approximations. We will discuss their validity, when testing our outcome in numerical simulations. With the spring constant κ we just calculate the force to 1st order around equilibrium, but there is no need to restrict ourselves to a linear force or parabolic potential respectively. Therefore the next section deals with details about the interaction potential.

2.4 Selecting a potential

For the Subcellular Element Model interaction potentials have to fulfil certain conditions. According to NEWMAN [New07] these are being

- 'repulsive at short distances' to not collapse and shrink to a point,
- 'weakly attractive over slightly longer scales' to stays compact,
- 'essentially zero (...) beyond a moderate scale' to let two isolated cells feel no attraction and
- inharmonic to allow 'elements to smoothly release each other under larger forces, such as during cell division or cell migration'.

The last argument shall not be of interest since we just want to model elasticity. There are of course a lot of possibilities and from NEWMAN's point of view the precise shape of

the potential does not affect cell mechanics - at least semi-quantitative. As an example we will have a look at the potential SANDERSIUS and NEWMAN used for testing their formula from the simple cubic approach [SN08]. The parabola potential shall be subject of our studies as well.

2.4.1 Modified Morse potential

A standard potential to model inter-molecular interactions in physics or chemistry is named after MORSE [Sch68] and reads

$$V_{\text{MORSE}}(r) = u_0 e^{-2\rho(r-r_{eq})} - 2u_0 e^{-\rho(r-r_{eq})}.$$

In the SEM publication [SN08] the exponential terms are replaced by GAUSSIAN functions, because of their steeper decay. The modified MORSE potential has the form

$$V(r) = u_0 e^{2\rho\left(1-\frac{r^2}{r_{eq}^2}\right)} - 2u_0 e^{\rho\left(1-\frac{r^2}{r_{eq}^2}\right)}. \quad (2.4.1)$$

The parameter u_0 controls the potential depth. The radius r_{eq} is the distance to the energy minimum and ρ varies the slope. Figure 2.4.1 helps to understand the influence of ρ on the scaled potential $V(r)/u_0$ and the scaled force $F(r)r_{eq}/u_0$, which are parameter independent. The force $F(r)$ reads

$$\begin{aligned} F(r) &= -\nabla_r V(r), \\ &= -\frac{4u_0\rho}{r_{eq}^2} r \left(1 - e^{\rho\left(1-\frac{r^2}{r_{eq}^2}\right)}\right) e^{\rho\left(1-\frac{r^2}{r_{eq}^2}\right)}. \end{aligned} \quad (2.4.2)$$

To combine this force field with $\kappa(E)$ of each scenario we linearise $F(r)$ around r_{eq} and identify κ , thus being able to calculate $u_0(E)$ and fully determine the potential:

$$\begin{aligned} T_{F,r=r_{eq}}^{(1)}(r) &= -8 \underbrace{\frac{u_0\rho^2}{r_{eq}^2}}_{=\kappa} \cdot (r - r_{eq}) \\ \kappa &= 8 \frac{u_0\rho^2}{r_{eq}^2} \end{aligned} \quad (2.4.3)$$

This potential fulfils all demands, but with the aim to be quantitative we quickly identify a significant problem: Linearisation holds only in a very small area around r_{eq} . But this is actually on what we based our approaches. When having a higher value of ρ we

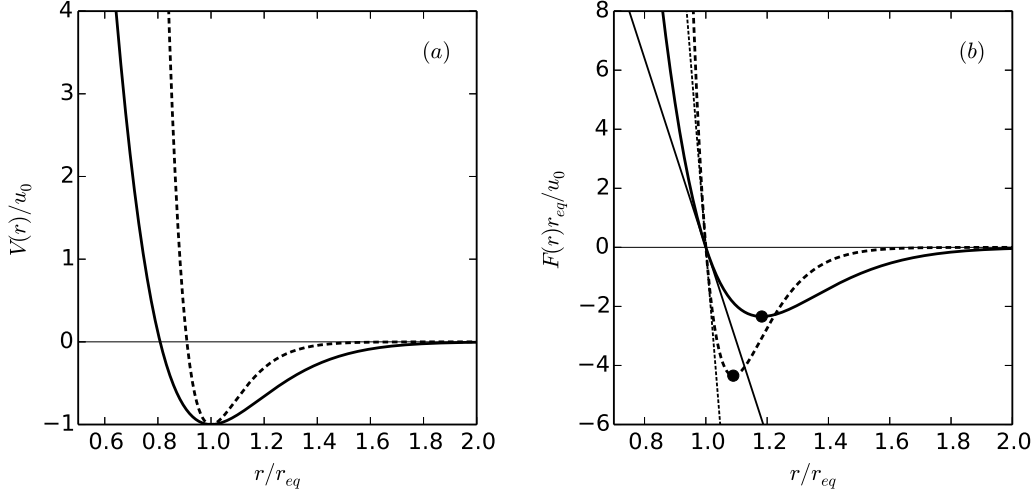


Figure 2.4.1: Scaled modified MORSE potential $V(r)/u_0$ in (a) on the left and associated force $F(r)r_{eq}/u_0$ in (b) on the right. Solid lines refer to $\rho = 2$ and dashed lines to $\rho = 4$. The black dots in (b) mark the inflection points of the potential $V(r)$. The tangents show the linear approximation at equilibrium.

might minimize the error but at once we get another problem. The inflection point, the point of maximum elongation, moves towards the equilibrium distance. This reduces the range of elongation, because interaction forces decrease and the modelled cell rips apart under a constant applied stress. With $\rho = 2$ the maximum elongation is about 20%, but for the value $\rho = 4$ the elongation cannot exceed 10%. Therefore, it might be useful to have a look at the parabola potential.

2.4.2 Parabola potential

A quadratic potential and its derived force as shown in Figure 2.4.2 have the simple form

$$V(r) = \frac{\kappa}{2}(r - r_{eq})^2 - V_0 \text{ and} \quad (2.4.4)$$

$$F(r) = -\kappa(r - r_{eq}). \quad (2.4.5)$$

These two equations shall be valid within a certain cutoff radius r_{cut} . If $r > r_{cut}$, then $V(r) = 0$ and also $F(r) = 0$. This cutoff can be determined by considering the next nearest neighbour distance being $2r_{eq}$ in 2D and $\sqrt{2}r_{eq}$ in 3D. To be equally able to compress and stretch the cell, we define the distance to the middle between nearest and

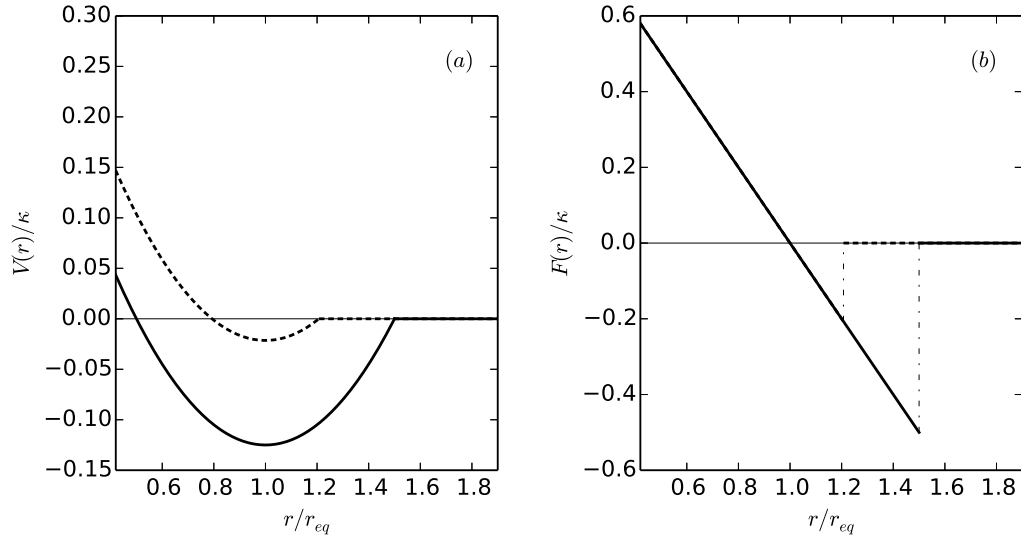


Figure 2.4.2: Scaled parabola potential $V(r)/\kappa$ in (a) on the left and associated force $F(r)/\kappa$ in (b) on the right. To show the different ranges depending on the dimension of space, 2D is illustrated with a solid line and dashed lines represent 3D. Notice that dashed lines are partly covered.

next nearest neighbours as r_{cut} .

$$\begin{aligned} r_{cut}^{2D} &= r_{eq} + \frac{2-1}{2}r_{eq} \\ &= \frac{3}{2}r_{eq} \end{aligned} \quad (2.4.6)$$

$$\begin{aligned} r_{cut}^{3D} &= r_{eq} + \frac{\sqrt{2}-1}{2}r_{eq} \\ &= \frac{\sqrt{2}+1}{2}r_{eq} \end{aligned} \quad (2.4.7)$$

To follow the convention $V(\infty) = 0$ one has to modify an offset V_0 according to the chosen r_{cut} .

Despite the smaller computational cost when comparing both force formulas 2.4.2 and 2.4.5, we find other advantages. For example, there is no error to our linearisation used in the derivation, because we chose the parabola on purpose. One also gains larger elongation, meaning about 21% in 3D and 50% in 2D. These benefits come along with the price of losing the smooth release of elements. Watching an SEM cell which rips apart in a movie provided in the publication [SN08], cell rupture appears to be modelled very well. But in fact, it is not clear what one actually can model beyond elasticity. In

contrast, this thesis will only focus on an area of strain, where our model more or less works, meaning the elastic modulus can be reproduced within a reasonable error.

3 Numerics

May the derivation of the previous chapter be reasonable and convincing, the need for an experimental validation is beyond dispute. Since the Subcellular Elements have no physical equivalent we cannot perform a real experiment. To test our results, we will simulate an SEM cell with a computer program. The following section deals with details about that program and the virtual experiment respectively. There will be one section about the solver used for the time integration. Afterwards, we will discuss the used set of parameters and how to deal with the measure of units will concern us. On a final note, we will find some words about the programming language.

But now we will give our attention to the explicit procedure of the experiment.

3.1 Experiment and pseudocode

Basically the experiment of determining a cell's elastic modulus is really simple. One needs the unstressed height of the arrangement as well as the height under stress. There are two different possibilities to achieve the latter. Either a well defined force is applied and the height is computed from the highest and lowest elements or the top elements are placed at a known height and the force acting on the entire system is computed after equilibration. For the second option we have start time evolution with elements distributed equally over the whole height otherwise top elements may be out of reach ($> r_{cut}$) for the layer of elements below. The simulation may even converge faster since elements are already almost at their final positions. However, in the first case less assumptions need to be made. Starting from the unstressed arrangement we really study the application of force to that SEM cell. This appears to be a more natural way.

We stay with the picture of a cell on a solid ground under stress. One needs to identify the bottom elements and fix them to the ground by setting their respective spatial component in every time step to zero. Stress shall be applied by a flat surface on top to which the cell adheres. This can be simulated by forcing all top elements always to have the same height. When equilibrium is reached, one can measure the height of the top elements and thus the elastic modulus can be computed. One can infer more

Algorithm 1 Measuring the elastic modulus of an SEM cell.

Input: We have to choose the number of dimensions D , the number of elements in i -direction N_i , the equilibrium distance r_{eq} , the time step size dt , the length of run tn , the strength of force f^* and the input elastic modulus E_{IN} . Furthermore the we need to specify a potential and provide the function $\text{GRADV}(r)$ with all its parameters.

```

1: function FORCE( $x, N, r_{cut}, \text{GRADV}$ )    ▷ calculate the force between all elements
2:   if periodic boundary then
3:     if  $x$  closer than  $r_{cut}$  to boundary then
4:       CREATE( $x_{Ghost}$ )                    ▷ create ghost elements
5:        $x \leftarrow x + x_{Ghost}$ 
6:        $r_{ij} \leftarrow x_i - x_j^T$                 ▷ compute distance matrix
7:        $f_{ij} \leftarrow -\text{GRADV}(r_{ij})$         ▷ compute potential gradient
8:        $f_{ii} \leftarrow 0$                         ▷ set self interaction to zero
9:        $f_{ij} \leftarrow f_{ij} \cdot (r_{ij} < r_{cut})$   ▷ apply cutoff radius
10:       $F_i \leftarrow \sum_j f_{ij}$                 ▷ compute resulting force for each element
11:       $F_i \leftarrow F_i[i \leq N]$               ▷ neglecting ghosts
12:      return  $F_i$ 
13:
14: function EULER( $x, tn, f^*, N, r_{cut}, h, \text{GRADV}$ )    ▷ calculate time evolution
15:    $xt[0] \leftarrow x$ 
16:   while  $t \leq tn$  do
17:      $v \leftarrow \text{FORCE}(xt[t], N, r_{cut}, \text{GRADV})$ 
18:      $v[ind_{top}] \leftarrow v[ind_{top}] + f^*$         ▷ apply force to top
19:      $xt[t + 1] \leftarrow xt[t] + v \cdot dt$ 
20:      $xt[t + 1, ind_{bottom}, h] \leftarrow 0$         ▷ fix bottom
21:      $xt[t + 1, ind_{top}, h] \leftarrow \frac{xt[t + 1, ind_{top}, h]}{2}$     ▷ average height of top
22:      $t \leftarrow t + 1$ 
23:   return  $xt$ 
24:
25:  $x \leftarrow$  initial position    ▷ place elements at position of force free equilibrium
26:  $N \leftarrow$  some function of  $N_i$     ▷ see caption of figure 2.3.1, 2.3.3, 2.3.5 and 2.3.7
27:  $r_{cut} \leftarrow \frac{3}{2}r_{eq}$  (2D) or  $\frac{\sqrt{2}+1}{2}r_{eq}$  (3D)    ▷ see equation 2.4.6 and 2.4.7
28:  $h \leftarrow y$  (2D) or  $z$  (3D)    ▷ component of axis aligned with the height
29:  $xt \leftarrow \text{EULER}(x, tn, f^*, N, r_{cut}, h, \text{GRADV})$     ▷ time evolution
30:  $\sigma \leftarrow \frac{f^*}{r_{eq}}$  (2D) or  $\frac{f^*}{r_{eq}^2}$  (3D)    ▷ see equation 2.3.1 and 2.3.7, compute stress
31:  $\epsilon \leftarrow (xt[tn, ind_{top}, h] - xt[0, ind_{top}, h]) / xt[0, ind_{top}, h]$     ▷ compute strain
32:  $E_{OUT} \leftarrow \sigma / \epsilon$ 
33: output  $E_{OUT}$ 

```

details from Algorithm 1, where the whole procedure is illustrated as a pseudocode. To model the speed of reaching equilibrium one needs to adjust the viscous damping constant¹[SN08]. We will set $\eta = 1$ since dynamic behaviour is not relevant to elasticity.

3.2 Solver

A time integration needs to be performed to solve the differential equations for a single SEM cell $\eta \dot{\mathbf{x}}_\alpha = \xi_\alpha - \nabla_\alpha \sum_{\beta \neq \alpha} V(|\mathbf{x}_\alpha - \mathbf{x}_\beta|)$. As seen already in algorithm 1, the EULER scheme is used for resolving this issue. To justify this choice we consider 10^3 elements, meaning without a smart domain decomposition we have to call $\mathbf{F}(r)$ at least 10^3 times per time step. The simple EULER solver

$$\mathbf{x}_{t+1} = \mathbf{x}_t + \mathbf{F}(r_t) \cdot dt \quad (3.2.1)$$

may not be very precise compared for example with the 4th order RUNGE-KUTTA scheme [PTVF07], but fast since it has minimal number of function calls. Precision is in our special case no problem. We just simulate the convergence to a minimum which does not depend on dynamics, but on the distances between elements. For that reason, the EULER method is a reasonable choice for this time evolution. At the end of each equilibration, oscillations around the true converged positions occur when the time step dt is chosen too large. This size is also often limited by the fact that elements destroy the close-packed order of the arrangement, when moving too far in one time step. By reducing its size oscillations disappear, a smooth movement is guaranteed and an unavoidable numerical error ensues. We estimate its order of magnitude with a test run. Two elements with the initial distance $1.5r_{eq}$ are left to equilibrate. Subtracting the final distance r_f from the theoretical value r_{eq} gives the error due to the chosen EULER solver. In Table 3.2.1 the result is shown for different time step sizes dt . Surprisingly the errors increase with a smaller dt . As can easily be seen from the EULER definition 3.2.1 and the values of the table, the spatial step $dx = |\mathbf{F}(r_f)| \cdot dt$ is of order 10^{-17} . Thus being smaller than machine precision elements cannot move any further - the numerical equilibrium is reached. In most cases a good choice for a large, but still not order destroying value for dt is 3.14×10^{-3} with an error $|r_{eq} - r_f| = 2.7 \times 10^{-15}$. We need to keep that in mind when later discussing about possible sources of error.

¹See the fundamental SEM equation 1.0.1 and 1.0.2

dt	$ r_{eq} - r_f $	$ \mathbf{F}(r_f) $
1×10^{-2}	8.9×10^{-16}	2.7×10^{-15}
1×10^{-3}	8.9×10^{-15}	2.7×10^{-14}
1×10^{-4}	9.0×10^{-14}	2.8×10^{-13}

Table 3.2.1: The numerical error arising from using the EULER solver depends on the time step size dt . r_f is the distance between two elements after reaching computational equilibrium. The theoretical value r_{eq} is set to 1.

3.3 Parameters

Of course, we simulate in order to compare our results later on with actual physical measurements. That means parameters should have reasonable values. Basically, there are the number of elements in every dimension N_i , the equilibrium distance r_{eq} , the applied force f^* and the input elastic modulus E_{IN} . Hence, the parameter space has five or six dimensions and is therefore tricky to explore. Setting all parameters but one to a standard value and vary the remaining one, makes it possible to plot the variation against the measured elastic modulus E_{OUT} in a clear 2D plot.

As in any numerical simulation, we need to define units of measure for all quantities. The following consideration leads us to the size of these units and the standard value of our parameters: For the sake of a short runtime we will always try to take the smallest number for N_i , which leads to a satisfying error. To come right to the point: N_i is of order 10^1 . The size of biological cells can vary a lot, but with the choice $l \approx 10 \mu\text{m}$, which is roughly the size of a red blood cell, we are somewhere in the right scale. Letting a unit of length (UL) equal one micron the standard value for $r_{eq} = \frac{l}{N_i} = 1 \text{ UL}$. The elastic modulus of a living cell is in the order of 100 Pa to 1000 Pa ([LFS⁺06],[MSO05],[BMS99],[DRSA05a]). Assumed $E_{IN} = 100 \text{ UF/UL}^2$ (unit of force per unit of length squared), one has the advantage of estimating the percentage error easily and can let the standard value of $E_{IN} = 100 \text{ UF/UL}^2 = 100 \text{ Pa}$. The unit of force has to be adjusted to fulfil this condition; from it we derive $1 \text{ UF} = 10^{-12} \text{ N}$. Notice that in 2D $E_{IN} = 100 \text{ UF/UL}$ thus $1 \text{ UF} = 10^{-6} \text{ N}$. The standard f^* should be a weak force so the cell stretches just a little. Otherwise we may get into trouble arising from the approximations we made. To be on the safe side we let $f^* = 10^{-3} \text{ UF}$ and apply stress of 10^{-3} Pa so that ϵ should be in the order of $\approx 10^{-5}$. Note that we made the arbitrary choice of f^* being positive, meaning that we pull on the top. Table 3.3.1 collates standard values and unit of measures.

Parameter	Standard value	Unit of measure
r_{eq}	1 UL	1 UL=1 μm
f^*	10^{-3} UF	1 UF= 10^{-12} N
E_{IN}	100 UF/UL ²	1 UF/UL ² =1 Pa

Table 3.3.1: Unless otherwise stated r_{eq} , f^* and E_{IN} will always be set to their standard value given in this table.

3.4 Language

The program used for the following simulation runs is written in Python. Being a script language Python requires no compiling which makes testing the code pretty fast. Together with the intuitive library VPython the element movements can be visualized at the same time. For larger simulations a more performant language should be used. For example the SEM client of the 'MOSAIC' group which is written in FORTRAN95. This code uses the 'Parallel Particle Mesh' (PPM) library which was developed from the same group [SWB⁺06, ADS10, AMRS13]. The client runs in parallel, thus it can achieve a much smaller run time. But since the code distributes different cells to different processors single cell experiments still run on only one core. In this work, the elastic modulus of single cells is computed and thus, the Python language is used without significant loss of computational time.

4 Results

At the transition from 'numerics' to this chapter a lot of computation was done using the SEM program. The elastic modulus has been calculated in two and three dimensions, with and without periodic boundaries for different parameters, namely the number of elements in each dimension, the equilibrium distance, the applied force and the theoretical elastic modulus we want to model. We will initially start with parameter standard values and find smallest acceptable values for element numbers N_i . To explore the parameter space we will proceed with varying all parameters one by one. According to the setup order we introduced in the theory chapter 2, one will find sections for each scenario containing results and plots of all associated simulation runs.

Also the two different shapes of the potential introduced in Section 2.4 will be checked for their impact on the elastic modulus. A comparison between them will be drawn on the basis of the periodic, two-dimensional HCP structure, hence right in the first section.

4.1 Periodic HCP in 2D and potential comparison

This section deals with the verification of the formula we derived for the two-dimensional case of a periodic, close-packed arrangement:

$$\kappa = \frac{4}{3\sqrt{3}}E_{IN}.$$

The elastic modulus we want to model is denoted by E_{IN} . In contrary there is the computed elastic modulus E_{OUT} . To recapitulate the scenery see Figure 2.3.1. Two potentials have been introduced in Section 2.4 and this will be the only arrangement in which we check their effect on the output. One has to pass the force field $\text{GRADV}(r)$ to Algorithm 1, which is Equation 2.4.5 for the parabola. For the modified MORSE potential we use Equation 2.4.2, where u_0 is determined by Equation 2.4.3.

As already mentioned there is the problem of a huge parameter space. To get started

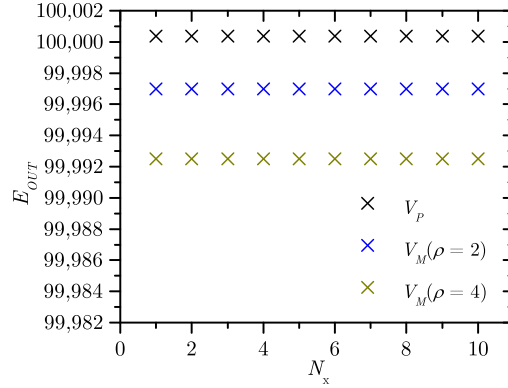


Figure 4.1.1: $E_{OUT}(N_x)$ graph of the periodic HCP in 2D. N_y is set to 6 and all other parameters have their standard value. Time steps are of size 3.33×10^{-3} . Black crosses belong to the parabola V_P and blue ($\rho = 2$) and dark yellow ($\rho = 4$) crosses to the modified MORSE potential V_M .

we let all parameters have their standard value and try to find the minimal, reasonable number of elements N_x and N_y . Starting with N_x we fix N_y at some point. For not hitting a special case we choose it not smallest possible, but for example $N_y = 6$. The result shown in Figure 4.1.1 illustrates that with the derived formula we are able to reproduce a given elastic modulus within the error of 0.0004 % to 0.008 % depending on the choice of the potential. The sources of error will be discussed in the next chapter. Since the system is periodic in x-direction the plot looks like expected and can be regarded as a validation of a proper implementation of ghost elements in the program.

With N_x having no influence on E_{OUT} we are free to choose $N_x = 1$ in the following simulations. This is what we do when testing the N_y influence - all other parameters remain the same. In Figure 4.1.2 (a) one gets the impression that E_{OUT} does not dependent on N_y . In fact the error increases exponentially as can be seen in (b) of the same figure. But with this order of magnitude it gives no occasion to revise the formula. The error may become relevant for huge numbers of N_y .

One can continue with varying the equilibrium distance r_{eq} using a minimal system size of $N_x = 1$ and $N_y = 2$. A meaningful range for this parameter might be from $r_{eq} = 10^{-2}$ UL to $r_{eq} = 10^2$ UL. For 1 UL=1 μm , this refers to a SEM cell with about 1000 elements of size 0.3 μm to 30 mm. Figure 4.1.3 illustrates the program output E_{OUT} in (a) and an exponentially decrease of the absolute error $\delta E = E_{OUT} - E_{IN}$ in (b). The error is still small enough to accept the result. But with an exponential influence, we see that r_{eq} has to be chosen wisely.

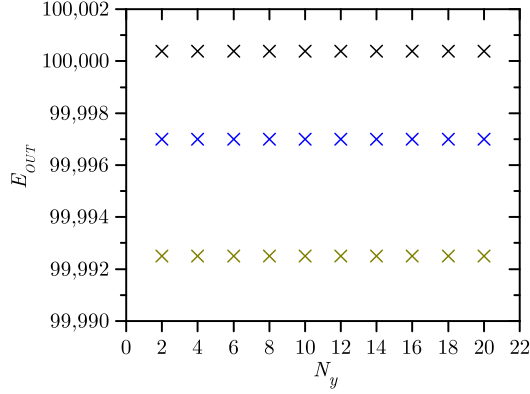
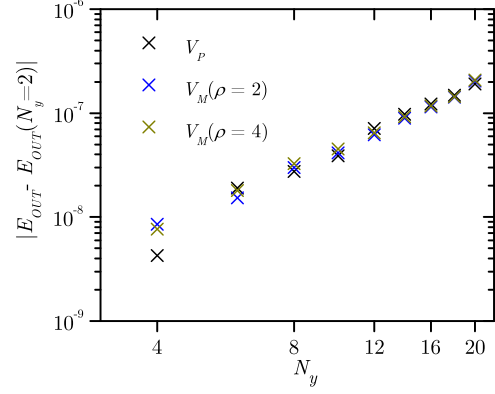
(a) N_y -dependence of E_{OUT} (b) Subtracting the first value of E_{OUT} with $N_y = 2$ from the data, an exponential error dependence on N_y becomes visible.

Figure 4.1.2: $E_{OUT}(N_y)$ graph in (a) and $|E_{OUT} - E_{OUT}(N_y = 2)|$ (N_y) graph in (b) of the periodic HCP in 2D. The legend is valid for both plots. $N_x = 1$ and all other parameters have their standard value.

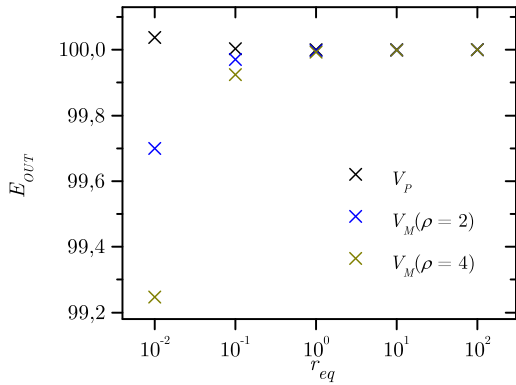
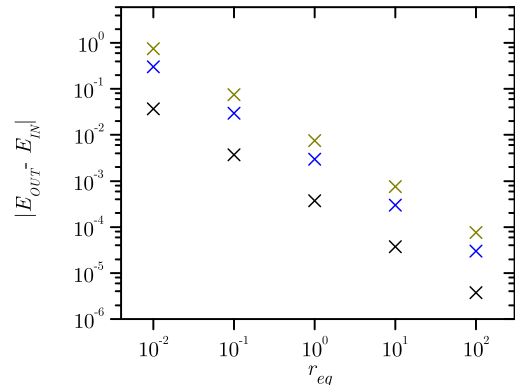
(a) r_{eq} -dependence of E_{OUT} (b) r_{eq} -dependence of the absolute error δE

Figure 4.1.3: $E_{OUT}(r_{eq})$ graph in (a) and $|E_{OUT} - E_{IN}|(r_{eq})$ graph in (b) of the periodic HCP in 2D. The legend is valid for both plots. The system has the size $N_x = 1$ and $N_y = 2$. All other parameters have their standard value.

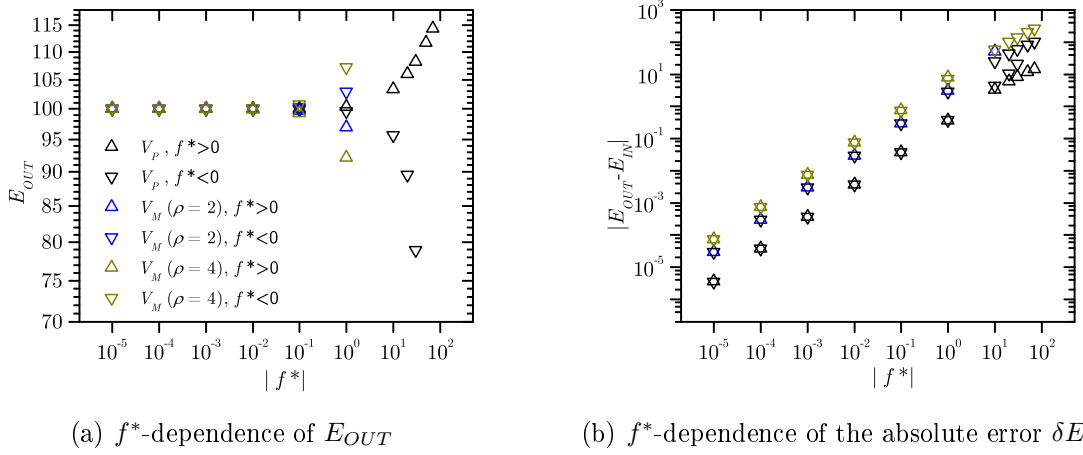
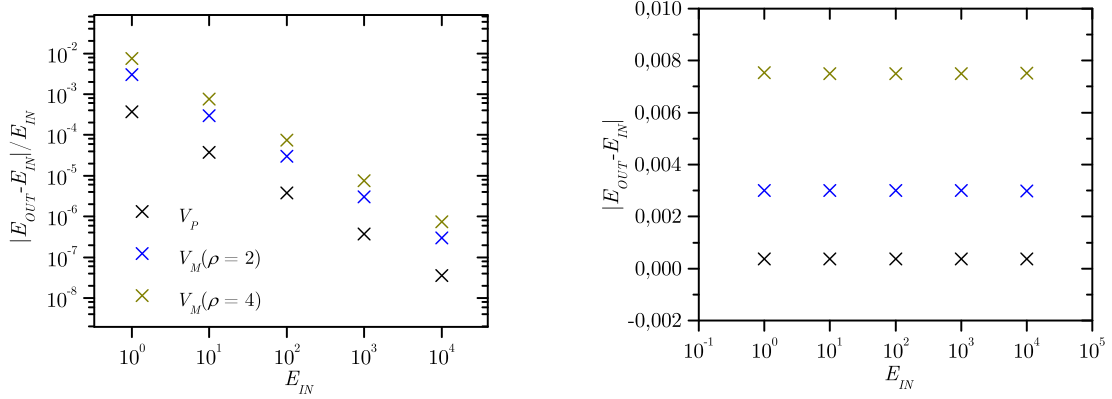


Figure 4.1.4: $E_{OUT}(f^*)$ graph in (a) and $|E_{OUT} - E_{IN}|(f^*)$ graph in (b) of the periodic HCP in 2D. The legend is valid for both plots. The system has the size $N_x = 1$ and $N_y = 2$. All other parameters have their standard value.

To study the force response, we measure E_{OUT} for f^* being positive and negative in the range from 10^{-5} UF to 10^2 UF. By doing so, we model the cell from a very small strain to breakage. Figure 4.1.4 shows the model behaviour. In the case of pulling ($f^* > 0$), the maximal elongation is reached when $r = r_{cut}$. For compressing ($f^* < 0$), the model fails if the y component of f starts to decrease with an increasing α , the angle between the force f and f^* .

Finally, one changes the stiffness of the SEM cell. We extend the already mentioned, reasonable range for a cell's elastic modulus and let E_{IN} take the values from 1 Pa to 10^4 Pa. With $1 \text{ Pa} = 1 \text{ UF} / \text{UL}^2$ the same values are used for computation. Figure 4.1.5 illustrates the relative error in (a) and the absolute error in (b). Since E_{IN} has no influence on the absolute error, the relative error decreases for larger values.

When comparing the potentials, the parabola gives always the best result. There are a couple of error contributions as we shall see in the next chapter (Chapter 5), but using the modified MORSE potential one gets a significant error in addition due to the fact that our approach is based on the parabola. Thus, the following simulations will employ the parabola potential. Furthermore, we can summarize that different potential shapes have no influence on the qualitative behaviour.



(a) E_{IN} -dependence of the relative error $\delta E/E_{OUT}$ (b) E_{IN} -dependence of the absolute error δE

Figure 4.1.5: The graph shows the relative error as a function of the modelled modulus E_{IN} in (a) and the absolute error in (b) of the periodic HCP in 2D. The legend is valid for both plots. The system has the size $N_x = 1$ and $N_y = 2$. All other parameters have their standard value.

4.2 Periodic FCC in 3D

For a three-dimensional close-packed arrangement, which is periodic in two dimensions, we derived the formula:

$$\kappa = \frac{r_{eq}}{\sqrt{2}} E_{IN}.$$

The related illustration is Figure 2.3.3. We will proceed by the analogy of the last section, in which also the sufficiency of only studying the parabola as force field potential has been established. Parameters are varied within the same range as in the two dimensional problem.

Starting with the system size, we arbitrary set $N_y = N_z = 3$ and vary N_x . The result is illustrated in Figure 4.2.1(a) and allows us to continue with $N_x = 1$, since E_{OUT} is constant for different N_x . For symmetry reasons the N_y -dependency, shown in Figure 4.2.1(b), looks the same and we let $N_y = 1$ for further simulations.

Varying N_z yields almost the same as we had for the N_y -dependency in the two dimensional case. In a reasonable range the error stays sufficiently small, though it increases exponentially as can be seen in Figure 4.2.2. Finding the elastic modulus to be independent of the system size, one can let $N_x = N_y = N_z = 1$ and test the

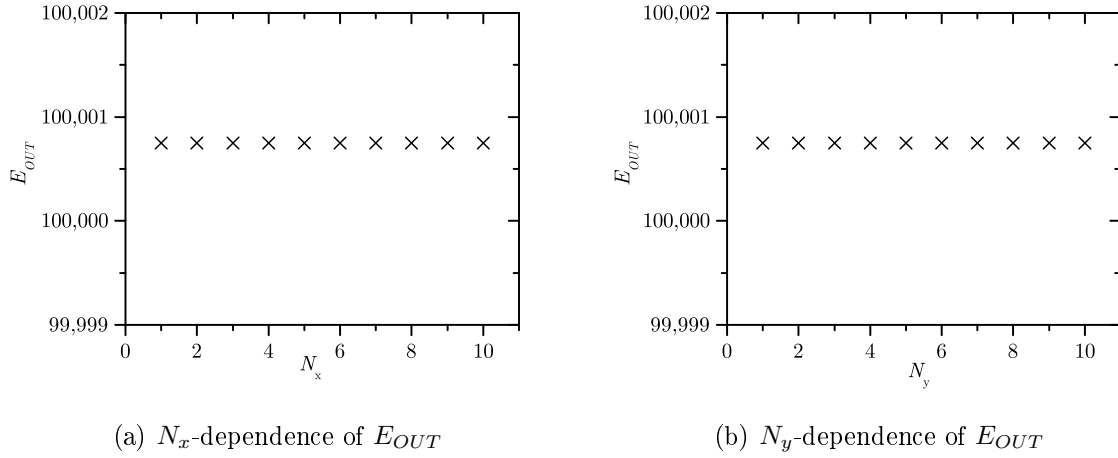


Figure 4.2.1: $E_{OUT}(N_x)$ graph in (a) and $E_{OUT}(N_y)$ graph in (b) of the periodic FCC in 3D. In (a) $N_y = N_z = 3$. In (b) $N_x = 1$ and $N_z = 3$. All other parameters have their standard value.

remaining parameters in a minimal runtime.

For the influence of r_{eq} we consider Equation 2.3.12 and remark that κ is a function of r_{eq} . In Figure 4.2.3(a) one finds the elastic modulus to be modelled considerable precise, except for very small r_{eq} . In fact, E_{OUT} seems to be an exponential function of r_{eq} as shown in Figure 4.2.3(b), which is much more sensitive than it has been in the last section. For roughly $r_{eq} \geq 10$ a numerical error occurs and δE stays almost constant.

When varying the applied force f^* , we get almost the same result as in the two dimensional case. Figure 4.2.4 illustrates the behaviour of E_{OUT} in (a) and of the absolute error δE in (b). As the force f^* is increased and the system gets closer to the point of breakage, the error in the elastic modulus increases significantly.

If one changes E_{IN} , one gets the result shown in Figure 4.2.5. The relative and absolute error plots look almost the same as in the HCP structure in 2D (Figure 4.1.5). With a constant absolute error we may get into trouble when modelling a very small elastic modulus. But staying in this reasonable range, our model works with a satisfying precision.

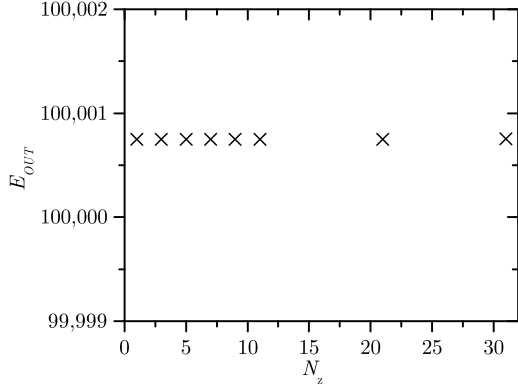
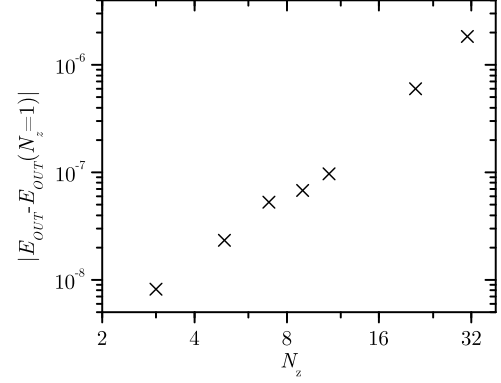
(a) N_z -dependence of E_{OUT} (b) Subtracting the first value with $N_z = 1$ from the rest, one gains a better insight in the N_z -dependence.

Figure 4.2.2: $E_{OUT}(N_z)$ graph in (a) and $|E_{OUT} - E_{OUT}(N_z = 1)|(N_z)$ graph in (b) of the periodic FCC in 3D. $N_x = N_y = 1$ and all other parameters have their standard value.

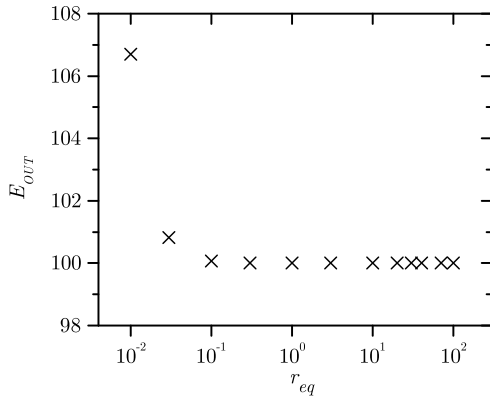
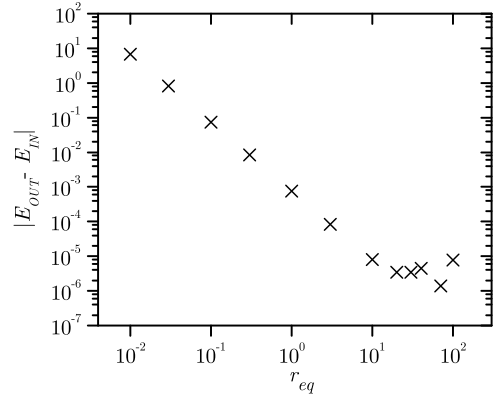
(a) r_{eq} -dependence of E_{OUT} (b) r_{eq} -dependence of the absolute error δE

Figure 4.2.3: $E_{OUT}(r_{eq})$ graph in (a) and $|E_{OUT} - E_{IN}|(r_{eq})$ graph in (b) of the periodic FCC in 3D. The system has the size $N_x = N_y = N_z = 1$. All other parameters have their standard value.

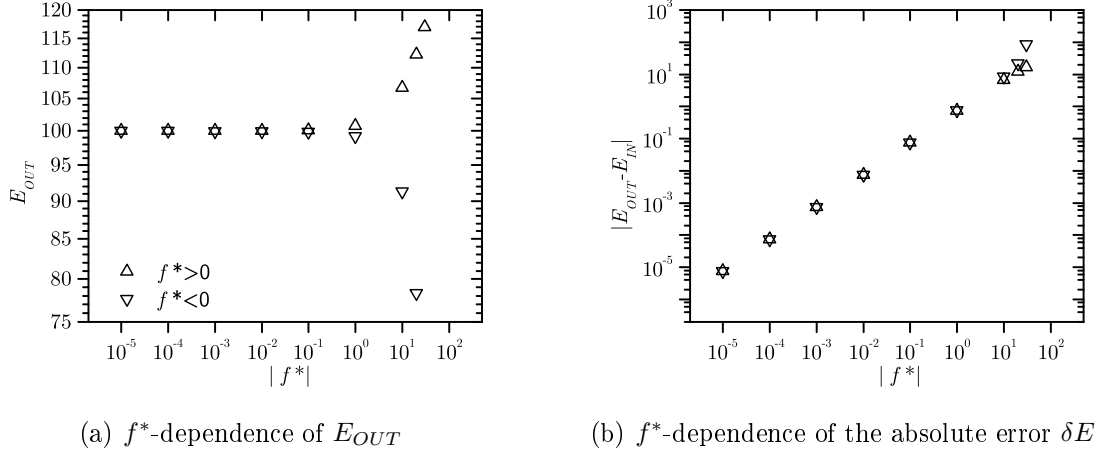


Figure 4.2.4: $E_{OUT}(f^*)$ graph in (a) and $|E_{OUT} - E_{IN}|(f^*)$ graph in (b) of the periodic FCC in 3D. The legend is valid for both plots. The system has the size $N_x = N_y = N_z = 1$. All other parameters have their standard value.

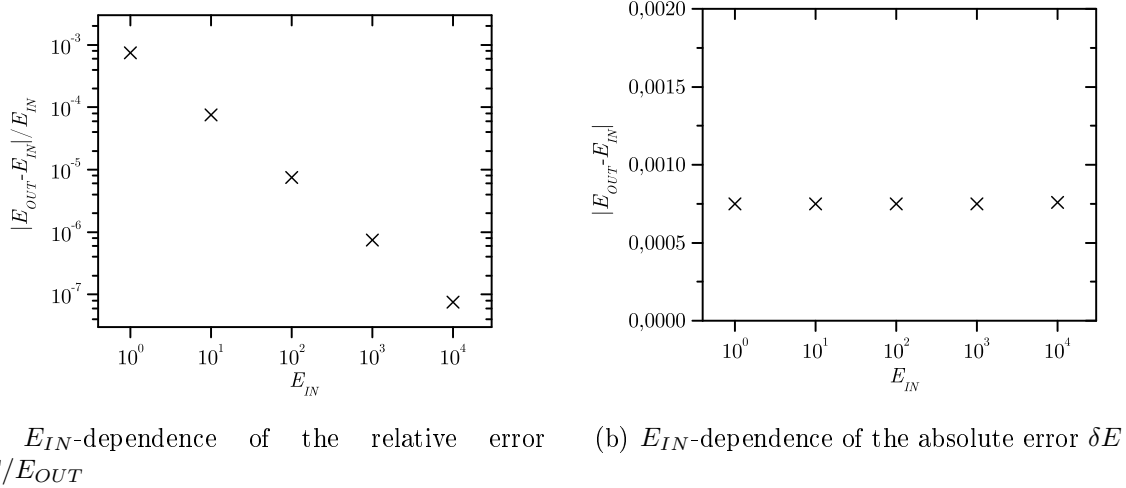


Figure 4.2.5: The graph shows the relative error as a function of the modelled modulus E_{IN} in (a) and the absolute error in (b) of the periodic FCC in 3D. The system has the size $N_x = N_y = N_z = 1$. All other parameters have their standard value.

4.3 Open HCP in 2D

In Section 2.3.3, we derived an approximate expression for κ (Equation 2.3.21) in the scenario of a two dimensional SEM-cell, where the computational domain is not periodic. An example arrangement is shown in Figure 2.3.1. We recall the formula:

$$\kappa = \frac{2}{3\sqrt{3}} (2 + w(N_x, N_y)) E_{IN} , \text{ where}$$

$$w(N_x, N_y) = \left[\frac{1}{4} \left(\frac{1}{8} \right)^{N_x-2} \left(\frac{1}{2} \right)^{N_y-2} \right]^{\frac{1}{N_x+N_y-3}} .$$

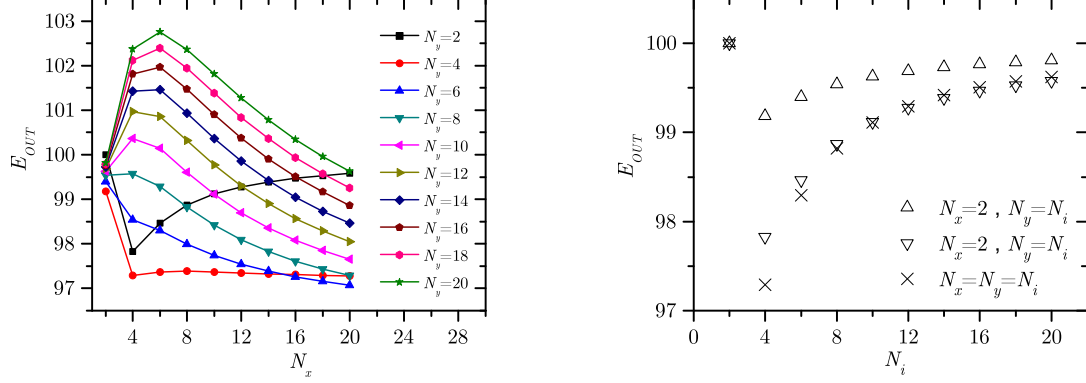
In this section, the theoretical outcome shall be tested numerically in the same manner as it has been done in the two previous sections. We will vary parameters in the same range.

We cannot look separately on the N_x - and N_y -dependency, because the curves for a constant N_y and a varied N_x differ considerably from each other. Therefore Figure 4.3.1 illustrates in (a) the data for N_x and N_y taking all even numbers up to 20. We remark that κ is derived by averaging different limits. Checking the validity of these limits can be done with the help of Figure 4.3.1(b). For N_x and N_y going independently and also at the same time to large values, the elastic modulus E_{OUT} seems to converge to the desired value $E_{IN} = 100$. Therefore, the maximal error for systems with intermediate values N_i of about 3% in the elastic modulus arises from the averaging process of the derived limits. With $N_x = N_y = 10$ the error in E_{OUT} is less than 1%, which is small enough for us to continue with this system size.

The equilibrium distance is varied and Figure 4.3.2 illustrates the result. In the modelled range, r_{eq} influences the elastic modulus just about 0,1%. But when taking smaller values beyond this range one has to be careful, because of the rapid increase for shrinking r_{eq} .

Enlarging the applied force gives almost the same result as in the previous scenarios of periodic HCP in 2D and periodic FCC in 3D as can be seen in Figure 4.3.3. As before, we find an exponential decrease in the elastic modulus E_{OUT} for shrinking f^* , but only down to a certain value of f^* and beyond that point the averaging error dominates, hence the absolute error stays constant.

We are left with testing the E_{IN} -dependence, which surprisingly shows a different behaviour than the one of E_{OUT} of the periodic scenarios, as illustrated in Figure 4.3.4. Here the absolute error is not constant, it rather increases exponentially as E_{IN} increases, meaning the relative error $|E_{OUT} - E_{IN}|/|E_{IN}|$ stays almost constant.



(a) N_x -dependence of E_{OUT} for different values N_y (b) Special cases of N_x and N_y -dependence of E_{OUT}

Figure 4.3.1: $E_{OUT}(N_x)$ graph for different values N_y in (a) and three special cases of N_x - and N_y -dependence of E_{OUT} in (b) of the open HCP in 2D. All other parameters have their standard value. For a better visualization data points are linked through coloured lines, but they do not have any physical or numerical meaning.

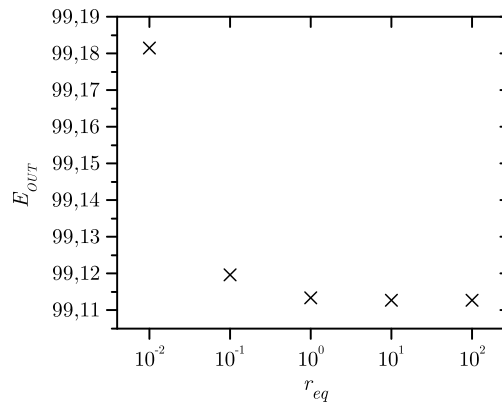


Figure 4.3.2: $E_{OUT}(r_{eq})$ graph of the open HCP in 2D. The system has the size $N_x = N_y = 10$. All other parameters have their standard value.

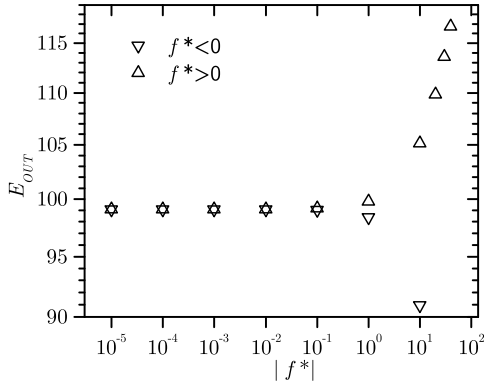
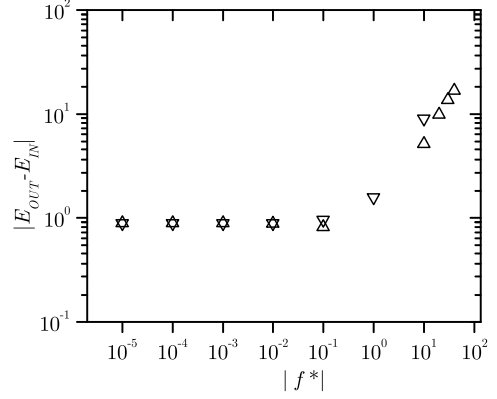
(a) f^* -dependence of E_{OUT} (b) f^* -dependence of the absolute error δE

Figure 4.3.3: $E_{OUT}(f^*)$ graph in (a) and $|E_{OUT} - E_{IN}|(f^*)$ graph in (b) of the open HCP in 2D. The legend is valid for both plots. The system has the size $N_x = N_y = 10$. All other parameters have their standard value.

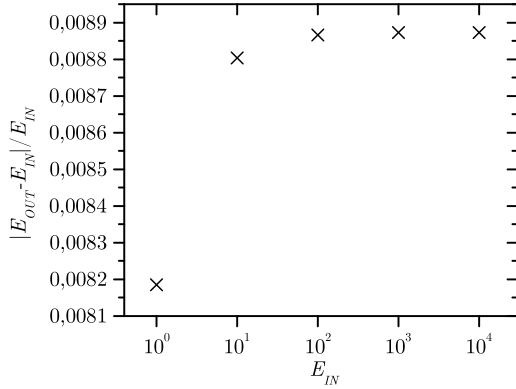
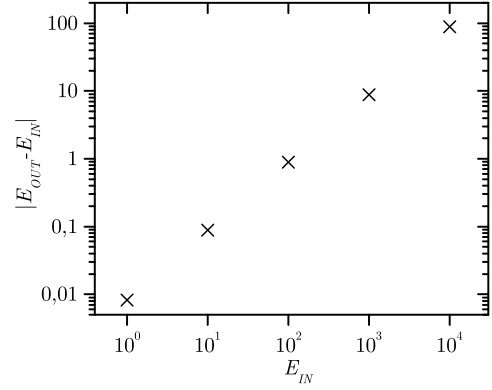
(a) E_{IN} -dependence of the relative error $\delta E/E_{OUT}$ (b) E_{IN} -dependence of the absolute error δE

Figure 4.3.4: The graph shows the relative error as a function of the modelled modulus E_{IN} in (a) and the absolute error in (b) of the open HCP in 2D. The system has the size $N_x = N_y = 10$. All other parameters have their standard value.

4.4 Open FCC in 3D

At last, we consider the three-dimensional face-centered cubic arrangement with open boundary conditions. For this system, illustrated in Figure 2.3.7, we have derived the following equation (Equation 2.3.31), which will be tested numerically in this section:

$$\kappa = \left(1 + \frac{1}{\sqrt{2}} w(N_x, N_y, N_z) \right) r_{eq} E_{IN} , \text{ where}$$

$$w(N_x, N_y, N_z) = \left[w(N_x, N_y, 1) (2w(N_x, N_y, 1))^{N_z-1} \right]^{\frac{1}{N_z}} \text{ and}$$

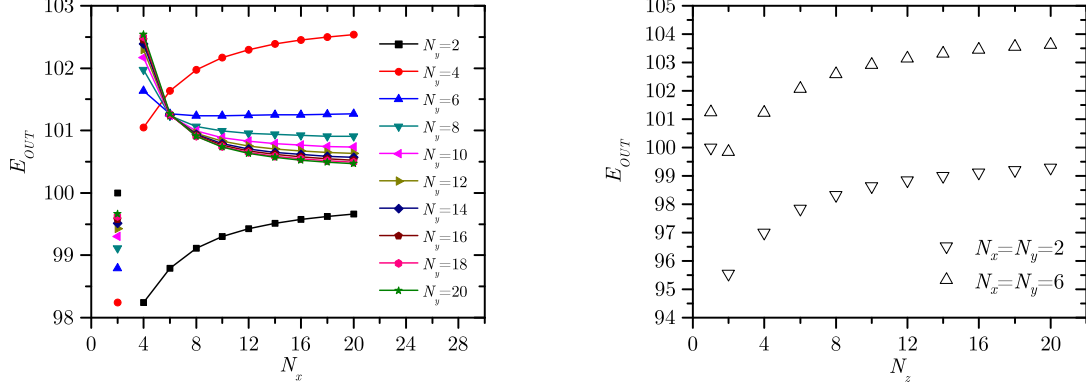
$$w(N_x, N_y, 1) = \frac{1}{\sqrt{2}} \frac{(N_x - 1)(N_y - 1)}{N_x N_y - \frac{1}{2}(N_x + N_y) + (N_x - 3)(N_y - 3)}.$$

Also in this case we expect a considerable error due to the process of averaging in z-direction and due to the way we derived $w(N_x, N_y, 1)$ for a single layer. To investigate these errors separately, we let $N_z = 1$ and vary N_x and N_y in the range from 2 to 20. The result is shown in Figure 4.4.1(a), where one sees that all limits ($E_{OUT}(N_x = 2, N_y = 2)$, $E_{OUT}(N_x = 2, N_y \rightarrow \infty)$, $E_{OUT}(N_x \rightarrow \infty, N_y = 2)$ and $E_{OUT}(N_x \rightarrow \infty, N_y \rightarrow \infty)$) seem to converge to E_{IN} . The weight $w(N_x, N_y, 1)$ is only valid if $N_x > 2$ and $N_y > 2$, otherwise the $(N_x - 3)(N_y - 3)$ term does not appear. Therefore the behaviour of E_{OUT} is different in these cases. For continuing the parameter investigation, we decide to let $N_x = N_y = 6$, which yields an error of about 1.2% for $N_z = 1$ at a short runtime. Now we fix N_x and N_y at 2 to examine only the N_z -dependency. Figure 4.4.1(b) illustrates that as $N_z \rightarrow \infty$ the elastic modulus seems to converge also in this case to the desired limit $E_{IN} = 100$. For the choice $N_x = N_y = 6$ the values of E_{OUT} when varying N_z are almost only shifted. This shift will be smaller and smaller, when increasing the number of elements in x- and y-direction. We want to continue with a cube and set $N_z = 6$ with an error of about 2.1%.

Figure 4.4.2 illustrates the behaviour of the elastic modulus when the equilibrium distance is varied in the range from $r_{eq} = 10^{-2}$ UL to $r_{eq} = 10^2$ UL. There is a strong decrease of the error up to certain value of $r_{eq} \approx 1$, when the error of N_z averaging and the one caused by $w(N_x, N_y, 1)$ start to dominate.

Stretching and compressing with different values of stress yield a very similar result as we had before in the periodic scenarios as well as in the open HCP in 2D. One can see from Figure 4.4.3, that the model fails when it comes to high values of f^* .

The last parameter left to check is the elastic modulus we want to simulate E_{IN} . With an exponentially increasing absolute error the relative error almost remains at about 2%, as visualized in Figure 4.4.4.



(a) N_x -dependence of E_{OUT} for different values N_y

(b) N_z -dependence of E_{OUT}

Figure 4.4.1: $E_{OUT}(N_x)$ graph for different values N_y while $N_z = 1$ in (a) and $E_{OUT}(N_z)$ graph in (b) of the open FCC in 3D. All other parameters have their standard value. For a better visualization data points are linked through coloured lines, but they do not have any physical or numerical meaning.

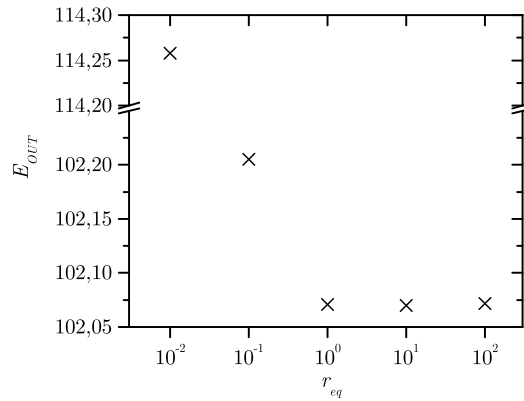


Figure 4.4.2: $E_{OUT}(r_{eq})$ graph of the open FCC in 3D. The system has the size $N_x = N_y = N_z = 6$. All other parameters have their standard value.

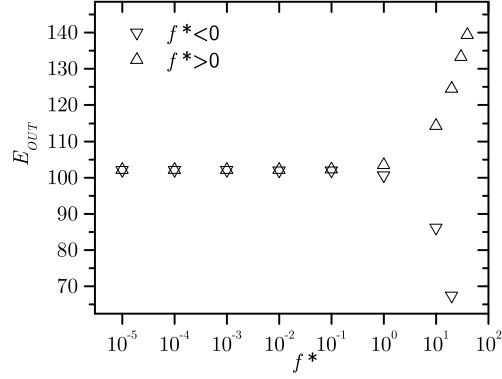
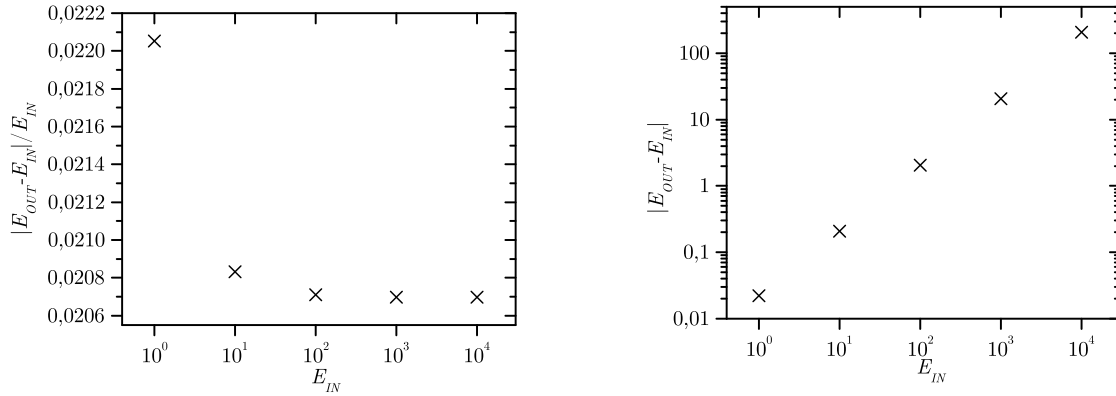


Figure 4.4.3: $E_{OUT}(f^*)$ graph of the open FCC in 3D. The system has the size $N_x = N_y = N_z = 6$. All other parameters have their standard value.



(a) E_{IN} -dependence of the relative error $\delta E/E_{OUT}$ (b) E_{IN} -dependence of the absolute error δE

Figure 4.4.4: The graph shows the relative error as a function of the modelled modulus E_{IN} in (a) and the absolute error in (b) of the open FCC in 3D. The system has the size $N_x = N_y = N_z = 6$. All other parameters have their standard value.

5 Error discussion

The numerical results of the previous chapter are afflicted with modelling errors. It was obvious from the very beginning that the elastic modulus will only be reproduced with a certain precision, which in fact changes remarkably from scenario to scenario. The aim of this chapter shall be the examination of error contributions, which is the basis for further improvements of the model.

If one recapitulates the derivation and the simulation, several possible sources of error occur. There are two numerical errors (the precision error δE^{prec} and the solver error δE^{solv}) and two systematic errors from approximating Δh ($\delta E^{\Delta h}$) and α (δE^α). Furthermore one has to consider the choice of the interaction potential (δE^{pot}) and, for non-periodic arrangements, the factor w causes an error (δE^w). Therefore the most general error $\delta E = |E_{OUT} - E_{IN}|$ reads:

$$\delta E = \delta E (\delta E^{prec}, \delta E^{solv}, \delta E^{pot}, \delta E^\alpha, \delta E^{\Delta h}, \delta E^w). \quad (5.0.1)$$

Doing a numerical experiment, no matter how much memory is assigned, the precision of each parameter or variable is limited. Sometimes, this circumstance can result in a considerable error - but not for the models presented in this thesis, because the dynamics do not at all depend on machine precision. The impact of the precision error is largest on the solver error δE^{solv} , when it limits the smallest spatial step (Table 3.2.1). And of course we compute the elastic modulus as a 32-bit float number, thus it cannot be infinitely precise. In the following we will not consider δE^{prec} , because it is very small compared to the other contributions.

First, we explain the errors of the two-dimensional HCP structure with periodic boundary conditions. In this case, $\delta E^w = 0$ and we write the absolute error δE as a sum of independent error contributions:

$$\delta E = \delta E^{solv} + \delta E^{pot} + \delta E^\alpha + \delta E^{\Delta h}. \quad (5.0.2)$$

This error is also shown in Figure 4.1.1.

5.1 Solver error: δE^{solv}

The solver error δE^{solv} is defined by the EULER solver. The time step is of size 3.14×10^{-3} , which results in a distance error between elements of $\delta r = 2.7 \times 10^{-15}$. With this information one calculates the error of length computes to $\delta l \approx (N_y - 1) \frac{\sqrt{3}}{2} \delta r$. Thus, the numerical contributions to the error are roughly:

$$\begin{aligned}
 \delta E^{num} &\approx \left| \frac{\sigma}{\epsilon^2} \right| \delta \epsilon \quad \text{with } \delta \epsilon = \frac{\delta l}{l} = \frac{\delta r}{r_{eq}} \text{ and } E = \frac{\sigma}{\epsilon} \\
 &\approx \left| \frac{E^2}{\sigma} \right| \frac{\delta r}{r_{eq}} \\
 &\approx \left| \frac{10^4}{10^{-3}} \right| 2.7 \times 10^{-15} \\
 &\approx 2.7 \times 10^{-8}
 \end{aligned} \tag{5.1.1}$$

With this order of magnitude the solver cannot be the reason for the observed error of $\delta E = 4 \times 10^{-4}$ as seen in Figure 4.1.1. Even if we have to change the step size, this error will always remain beyond our interest.

5.2 Fixed-angle approximation: δE^α

For δE^α , we remember the derivation of the stress σ where the assumption $f^* = 2f \cos(\alpha)$ with $\alpha = 30^\circ$ was made. Indeed α has a f^* dependency and therefore its value varies around 30° . To get an idea of δE^α one calculates $\left| \frac{dE}{d\cos(\alpha)} \right| \delta \cos(\alpha)$ where $\delta \cos(\alpha) = \cos(\alpha) - \cos(30^\circ)$. After each simulation run α is known and can be computed by

$$\begin{aligned}
 \alpha(\epsilon) &= \tan^{-1} \left(\frac{r_{eq}}{2} \frac{2}{\sqrt{3}(1+\epsilon)r_{eq}} \right) \\
 &= \tan^{-1} \left(\frac{1}{\sqrt{3}(1+\epsilon)} \right).
 \end{aligned}$$

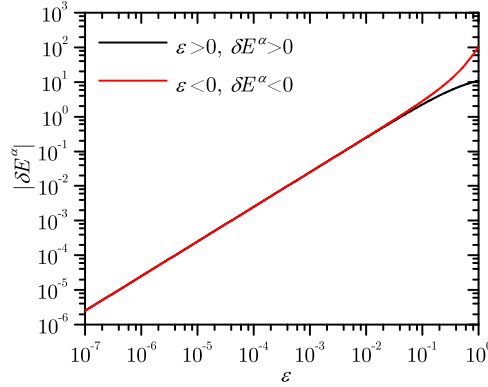


Figure 5.2.1: The error arising from the fixed-angle approximation δE^α . Shown is the plot of Equation 5.2.3 for positive strain ϵ in black and in red for negative strain ϵ respectively.

One calculates straight forward:

$$\delta \cos(\alpha) = \frac{\sqrt{3}}{2} - \cos\left(\tan^{-1}\left(\frac{1}{\sqrt{3}(1+\epsilon)}\right)\right) \quad \text{and} \quad (5.2.1)$$

$$\delta E^\alpha = \left| \frac{d}{d \cos(\alpha)} \left(\frac{\sigma}{\epsilon} \right) \right| \delta \cos(\alpha) \quad (5.2.2)$$

$$\begin{aligned} &= \left| \frac{d}{d \cos(\alpha)} \left(\frac{2 \cos(\alpha) f}{A \epsilon} \right) \right| \delta \cos(\alpha), \\ &= \left| \frac{2f}{A \epsilon} \right| \delta \cos(\alpha), \\ &\approx \left| \frac{E}{\cos(30^\circ)} \right| \delta \cos(\alpha). \end{aligned} \quad (5.2.3)$$

Figure 5.2.1 illustrates this function and for the current situation with standard values of $\epsilon \approx 10^{-5}$. The fixed-angle error becomes $\delta E^\alpha \approx 2 \times 10^{-4}$. The fixed-angle approximation turns out to be a proper candidate for the error that we see in Figure 4.1.1.

5.3 Linear elongation approximation: $\delta E^{\Delta h}$

Another contribution to the error occurs due to the Δh approximation. It became necessary when we expressed the height Δh as a linear function of Δr , the elongation between elements. One can estimate the size of $\delta E^{\Delta h}$ by calculating $\left| \frac{dE}{d\Delta h} \right| \delta h$. We define δh as the difference between the actual Δh^a and Δh^T which is the TAYLOR

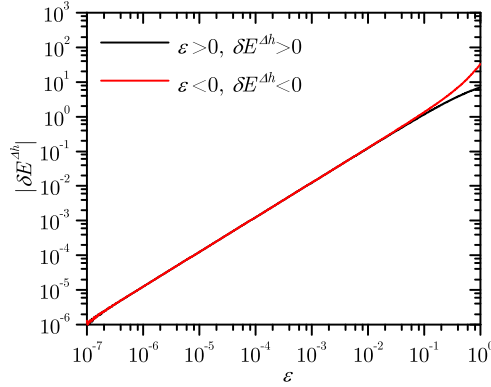


Figure 5.3.1: The error arising from the Δh TAYLOR expansion $\delta E^{\Delta h}$. Shown is the plot of Equation 5.3.2 for positive ϵ in black and in red for negative ϵ respectively.

approximation. As can be seen easily $\Delta h^a = -\epsilon \frac{\sqrt{3}}{2} r_{eq}$. For Δh^T we make use of this result, plug it into PYTHAGORAS' theorem 2.3.3 and get the value for Δr

$$\Delta r = \left(1 - \frac{\sqrt{3}}{2} \sqrt{(1 + \epsilon)^2 + \frac{1}{3}} \right) r_{eq}. \quad (5.3.1)$$

With the TAYLOR expansion $\Delta h^T = \frac{2}{\sqrt{3}} \Delta r$ (Equation 2.3.4) we write the error $\delta E^{\Delta h}$ as a function of ϵ in the following form:

$$\begin{aligned} \delta E^{\Delta h} &= \left| \frac{dE}{d\Delta h} \right| \delta h \\ &= \left| \frac{d}{d\Delta h} \left(\frac{\sigma l_0}{(N_y - 1)\Delta h} \right) \right| (\Delta h^a - \Delta h^T) \\ &= \left| \frac{E}{\Delta h} \right| \left(-\epsilon \frac{\sqrt{3}}{2} r_{eq} - \frac{2}{\sqrt{3}} \left(1 - \frac{\sqrt{3}}{2} \sqrt{(1 + \epsilon)^2 + \frac{1}{3}} \right) r_{eq} \right) \\ &= \left| \frac{2}{\sqrt{3}} \frac{E}{\epsilon r_{eq}} \right| \left(-\epsilon \frac{\sqrt{3}}{2} - \frac{2}{\sqrt{3}} + \sqrt{(1 + \epsilon)^2 + \frac{1}{3}} \right) r_{eq} \\ &= \left| \frac{E}{\epsilon} \right| \left(\frac{2}{\sqrt{3}} \sqrt{(1 + \epsilon)^2 + \frac{1}{3}} - \frac{4}{3} - \epsilon \right) \end{aligned} \quad (5.3.2)$$

Figure 5.3.1 illustrates the function graph, which looks surprisingly similar to the one of $\delta E^\alpha(\epsilon)$. Indeed, the error $\delta E^{\Delta h}$ for the actual case where $\epsilon = 10^{-5}$ is about 10^{-4} . We see that the linear elongation approximation contributes significantly to the total error δE .

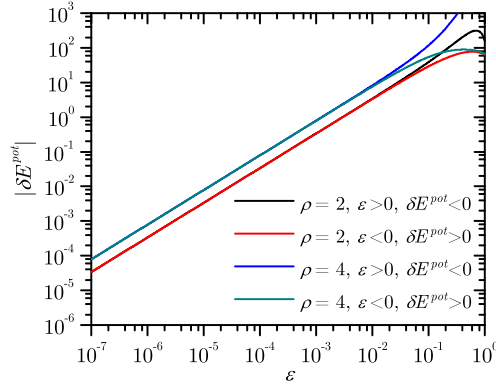


Figure 5.4.1: The error arising from the choice of the potential δE^{pot} . Shown is the plot of Equation 5.4.1 for $\rho = 2$ and $\rho = 4$ in the case of stretching ($\epsilon > 0$) and compressing ($\epsilon < 0$).

5.4 Parabolic potential approximation: δE^{pot}

Since our approach is based on linear forces, meaning the parabola potential, we find an additional source of error δE^{pot} . We examine the influence of the force f by calculating $\left| \frac{dE}{df} \right| \delta f$ where $\delta f = f_P(r_{eq} + \Delta r) - f_M(r_{eq} + \Delta r)$. In order to compare this error with those described previously, we express δf in terms of ϵ . To derive the full equation we need the force fields f_P (2.4.5) and f_M (2.4.2). Using the $u_0(\kappa)$ relation (2.4.3) we can insert the κ expression 2.3.6 in both force fields. Replacing Δr with Equation 5.3.1 yields the entire $\delta f(\epsilon)$, which is not be given here, because of its length. The error δE^{pot} reads

$$\begin{aligned}
 \delta E^{pot} &= \left| \frac{d}{df} \left(\frac{2 \cos(\alpha) f}{A \epsilon} \right) \right| \delta f(\epsilon) \\
 &\approx \left| \frac{2 \cos(30^\circ) E}{f^*} \right| \delta f(\epsilon) \text{ with } E = \frac{f^*}{r_{eq} \epsilon} \text{ and } \cos(30^\circ) = \frac{\sqrt{3}}{2} \\
 &\approx \left| \frac{\sqrt{3}}{r_{eq} \epsilon} \right| \delta f(\epsilon)
 \end{aligned} \tag{5.4.1}$$

Figure 5.4.1 shows the function $\delta E^{pot}(\epsilon)$ for the modified MORSE potential for $\rho = 2$ and $\rho = 4$. We notice that the error has the opposite sign compared to δE^α and $\delta E^{\Delta h}$, so they compensate each other partly. With a potential steeper than the parabola, the error would have been worse, since each contribution would have a positive sign. Look-

ing at $\epsilon = 10^{-5}$ for our actual case we have $\delta E_{\rho=2}^{pot} \approx 3.4 \times 10^{-3}$ and $\delta E_{\rho=4}^{pot} \approx 7.8 \times 10^{-3}$. Summing up the fixed-angle approximation, the linear elongation approximation and the parabolic potential approximation, it fits perfectly well with the error seen in Figure 4.1.1.

5.5 Weighting factor: δE^w

The error caused by the weighting factor w shall be discussed briefly using the example of the open FCC structure. We recall, that for a non-periodic arrangement the fact of having an asymmetry at the edges, forces us to introduce an averaged Δh . This is done by the factor $w(N_x, N_y, N_z)$.

There is no need to derive the error formulas from above also for this scenario. The measuring point in Figure 4.4.1(a) with $(N_x = N_y = 2, N_z = 1)$, gives us an indication of the error without δE^w . We easily see that w yields the major contribution. Since this problem exists due to the open boundaries, one can minimize the error by choosing large values for the number of elements N_x, N_y and N_z . Thus, the number of elements at the edges will be small compared with the number of elements from the interior of the modelled cell.

6 Summary

The aim of this thesis was to adjust the Subcellular Element Model in order to model the linear elasticity of cellular tissues at a quantitative level. We derived formulas for the spring constant of a linearised force. The most probable arrangement of subcellular elements, namely the close-packed configuration, has built the basis for this approach. Several approximations were made and their impact on the numerical result was discussed. We subsequently tested these formulas in a numerical single cell experiment using a computer program and explored the parameter space.

We are able to reproduce an elastic modulus with the SEM in the range of living cells ([LFS⁺06], [MSO05], [BMS99], [DRSA05a]). This is achieved in two and in three dimensions, with periodic and with open boundary conditions. But there are two restrictions:

- The first restriction occurs only in open boundary systems. The problem of asymmetry at the edges forces us to have a small surface to volume ratio in order to push the error δE^w down to the desired precision. On the one hand there is the positive aspect, that it is in fact possible to let this error shrink arbitrarily. But on the other hand the number of elements and thus the simulation runtime increases remarkably. As counteraction and of course for multicellular structures one should write the program differently, so it decomposes the computational domain, not to calculate all possible interactions, but important ones between neighbouring elements. Equipped with such a feature it can be run in parallel, thus the run will be considerable faster.
- The second restriction arises from the fixed-angle approximation and the linear elongation approximation, because they are only valid in a certain range of strain. Depending on the accuracy of the modelled elastic modulus the model fails at some point. For example, for $\epsilon \approx 10\%$, both relative errors, $\delta E^{\Delta h}/E$ and $\delta E^\alpha/E$, reach the size of about 1 % to 10 %. Stretching the SEM cell further, will lead to plastic breakage, meaning that the strain restriction becomes only relevant in a small range of strain. If we want to model living cells, which have been stretched by

DESPRAT *et al* to strain values of around 400% to 600% [DRSA05b], the SEM has to be extended. One attempt has been made by SANDERSIUS *et al* [SWN11] in which the authors introduced active subcellular elements which disappear in regions of low stress and appear in regions of high stress. In this way, they were able to stretch an SEM cell up to a strain value of 200%. However to further develop this model to a quantitative level will probably require some effort.

We also have to mention two drawbacks due to the weighting factor w , which are accordingly just relevant in open boundary scenarios:

- Since cells can change their shape, the number of subcellular elements in one dimension N_i can evolve in time. There are two possibilities to deal with the N_i -dependence of the weighting factor $w(N_x, N_y)$ in 2D and $w(N_x, N_y, N_z)$ in 3D. Either we are precise and update the numbers N_i from time to time for the price of a time dependent force field or we just let N_i scale with $\sqrt[D]{N}$, where D indicates the number of space dimensions. The second option will lead to an additional error, which should be small using a lot of subcellular elements per cell.
- Another drawback due to the introduction of the weighting factor w , is that it is not symmetric in the element numbers N_i . Hence we need to know in which direction the stress acts. In all other cases, than in these limited ones, one again must let N_i scale with $\sqrt[D]{N}$.

This work can be regarded as the basis of several positive future SEM improvements. The stress-strain relation should be extended with linear as well as non-linear elastic cell responses to finally model a cell in at higher strain values. This might be possible with an adaptive cut-off radius. For further mechanical force applications, also the shear modulus is an additional relevant quantity necessary to properly model deformation. But also shearing will have narrow limits, because all subcellular elements are equal, so they will be soon attracted by a next-nearest neighbour instead of tending to their initial position. The interesting question remains if one can set the elastic and shear modulus independent of each other, because in principle the force field was defined completely by focussing on YOUNG's modulus. Therefore, it may be necessary to take previous time steps into account or to introduce an anisotropic interaction potential, since the applied shear force acts orthogonal to the force for single axis elasticity.

A promising expansion for the SEM would be a combination with an active continuum theory, in order to model active processes without losing the achieved mechanical behaviour of this work. By defining a concentration field of a biomechanical fuel, such as

ATP, to model molecular motors, one could compute an additional force at the coordinates of each subcellular element. Afterwards from the elements movements, one could approximate a velocity field, which enters in the constitutive equation of the concentration field. Once such a hybrid framework exists, one can extend it with achievements from other successful continuum theories, like the active polar gel model by KRUSE *et al* [KJJ⁺05].

Bibliography

- [ADS10] AWILE, Omar ; DEMIREL, Ömer ; SBALZARINI, Ivo F.: Toward an Object-Oriented Core of the PPM Library. In: *Proc. ICNAAM, Numerical Analysis and Applied Mathematics, International Conference*, AIP, 2010, S. 1313–1316
- [AMRS13] AWILE, Omar ; MITROVIĆ, Milan ; REBOUX, Sylvain ; SBALZARINI, Ivo F.: A domain-specific programming language for particle simulations on distributed-memory parallel computers. In: *Proc. III Intl. Conf. Particle-based Methods (PARTICLES)*. Stuttgart, Germany, 2013, S. p52
- [BMS99] BAUSCH, A. R. ; MOLLER, W. ; SACKMANN, E.: Measurement of local viscoelasticity and forces in living cells by magnetic tweezers. In: *Biophys. J.* 76 (1999), Jan, Nr. 1 Pt 1, S. 573–579
- [Byr03] BYRNE, Helen M.: Modelling Avascular Tumour Growth. In: L. PREZIOS ed. (Hrsg.): *Cancer Modelling and Simulation*. Boca Rato : CRC Press, 2003
- [Cha00] CHAPLAIN, M. A.: Mathematical modelling of angiogenesis. In: *J. Neurooncol.* 50 (2000), Nr. 1-2, S. 37–51
- [DKKO95] DAVIDSON, L. A. ; KOEHL, M. A. ; KELLER, R. ; OSTER, G. F.: How do sea urchins invaginate? Using biomechanics to distinguish between mechanisms of primary invagination. In: *Development* 121 (1995), Jul, Nr. 7, S. 2005–2018
- [DKM95] DRASDO, D. ; KREE, R. ; MCCASKILL, J. S.: Monte Carlo approach to tissue-cell populations. In: *Phys Rev E Stat Phys Plasmas Fluids Relat Interdiscip Topics* 52 (1995), Dec, Nr. 6, S. 6635–6657
- [DRSA05a] DESPRAT, N. ; RICHERT, A. ; SIMEON, J. ; ASNACIOS, A.: Creep function of a single living cell. In: *Biophys. J.* 88 (2005), Mar, Nr. 3, S. 2224–2233

- [DRSA05b] DESPRAT, N. ; RICHERT, A. ; SIMEON, J. ; ASNACIOS, A.: Creep function of a single living cell. In: *Biophys. J.* 88 (2005), Mar, Nr. 3, S. 2224–2233
- [GG92] GRANER, F. ; GLAZIER, J. A.: Simulation of biological cell sorting using a two-dimensional extended Potts model. In: *Phys. Rev. Lett.* 69 (1992), Sep, Nr. 13, S. 2013–2016
- [Gri05] GRIMA, R.: *Ph.D. Thesis.* Arizona State University, 2005
- [IMW+01] IGOSHIN, O. A. ; MOGILNER, A. ; WELCH, R. D. ; KAISER, D. ; OSTER, G.: Pattern formation and traveling waves in myxobacteria: theory and modeling. In: *Proc. Natl. Acad. Sci. U.S.A.* 98 (2001), Dec, Nr. 26, S. 14913–14918
- [IVH10] INGOLF V. HERTEL, C.-P. S.: *Atome, Moleküle und optische Physik 2.* Springer, 2010. – ISBN 978–3–642–11973–6
- [KJJ+05] KRUSE, K. ; JOANNY, J. F. ; JULICHER, F. ; PROST, J. ; SEKIMOTO, K.: Generic theory of active polar gels: a paradigm for cytoskeletal dynamics. In: *Eur Phys J E Soft Matter* 16 (2005), Jan, Nr. 1, S. 5–16
- [LFS+06] LU, Yun-Bi ; FRANZE, Kristian ; SEIFERT, Gerald ; STEINHÄUSER, Christian ; KIRCHHOFF, Frank ; WOLBURG, Hartwig ; GUCK, Jochen ; JANMEY, Paul ; WEI, Er-Qing ; KÄS, Josef ; REICHENBACH, Andreas: Viscoelastic properties of individual glial cells and neurons in the CNS. In: *Proceedings of the National Academy of Sciences* 103 (2006), Nr. 47, 17759–17764. <http://dx.doi.org/10.1073/pnas.0606150103>. – DOI 10.1073/pnas.0606150103
- [MH01] MAREE, A. F. ; HOGEWEG, P.: How amoeboids self-organize into a fruiting body: multicellular coordination in *Dictyostelium discoideum*. In: *Proc. Natl. Acad. Sci. U.S.A.* 98 (2001), Mar, Nr. 7, S. 3879–3883
- [MSO05] MICOULET, A. ; SPATZ, J. P. ; OTT, A.: Mechanical response analysis and power generation by single-cell stretching. In: *Chemphyschem* 6 (2005), Apr, Nr. 4, S. 663–670
- [New05] NEWMAN, T. J.: Modeling multicellular systems using subcellular elements. In: *Math Biosci Eng* 2 (2005), Jul, Nr. 3, S. 613–624

- [New07] NEWMAN, TimothyJ.: Modeling Multicellular Structures Using the Subcellular Element Model. Version:2007. http://dx.doi.org/10.1007/978-3-7643-8123-3_10. In: ANDERSON, AlexanderR.A. (Hrsg.) ; CHAPLAIN, MarkA.J. (Hrsg.) ; REJNIAK, KatarzynaA. (Hrsg.): *Single-Cell-Based Models in Biology and Medicine*. Birkhäuser Basel, 2007 (Mathematics and Biosciences in Interaction). – DOI 10.1007/978-3-7643-8123-3_10. – ISBN 978-3-7643-8101-1, 221-239
- [PMO00] PAINTER, K. J. ; MAINI, P. K. ; OTHMER, H. G.: A chemotactic model for the advance and retreat of the primitive streak in avian development. In: *Bull. Math. Biol.* 62 (2000), May, Nr. 3, S. 501–525
- [PTVF07] PRESS, William H. ; TEUKOLSKY, Saul A. ; VETTERLING, William T. ; FLANNERY, Brian P.: *Numerical Recipes 3rd Edition: The Art of Scientific Computing*. 3. New York, NY, USA : Cambridge University Press, 2007. – ISBN 0521880688, 9780521880688
- [Rec90] RECKNAGEL, A.: *Physik: Mechanik*. Berlin : Verlag Technik, 1990
- [RJM05] RUBINSTEIN, B. ; JACOBSON, K. ; MOGILNER, A.: MULTISCALE TWO-DIMENSIONAL MODELING OF A MOTILE SIMPLE-SHAPED CELL. In: *Multiscale Model Simul* 3 (2005), Nr. 2, S. 413–439
- [SBGZ99] STOTT, E.L. ; BRITTON, N.F. ; GLAZIER, J.A. ; ZAJAC, M.: Stochastic simulation of benign avascular tumour growth using the Potts model. In: *Mathematical and Computer Modelling* 30 (1999), Nr. 5, 183 - 198. [http://dx.doi.org/http://dx.doi.org/10.1016/S0895-7177\(99\)00156-9](http://dx.doi.org/http://dx.doi.org/10.1016/S0895-7177(99)00156-9). – DOI [http://dx.doi.org/10.1016/S0895-7177\(99\)00156-9](http://dx.doi.org/10.1016/S0895-7177(99)00156-9). – ISSN 0895-7177
- [Sch68] SCHIFF, Leonard I.: *Quantum Mechanics*. 3rd ed. Singapore : McGraw-Hill, 1968
- [SN08] SANDERSIUS, S. A. ; NEWMAN, T. J.: Modeling cell rheology with the Subcellular Element Model. In: *Phys Biol* 5 (2008), Nr. 1, S. 015002
- [SWB⁺06] SBALZARINI, I. F. ; WALTHER, J. H. ; BERGDORF, M. ; HIEBER, S. E. ; KOTSALIS, E. M. ; KOUMOUTSAKOS, P.: PPM – A Highly Efficient Parallel Particle-Mesh Library for the Simulation of Continuum Systems. In: *J. Comput. Phys.* 215 (2006), Nr. 2, S. 566–588

- [SWN11] SANDERSIUS, S. A. ; WEIJER, C. J. ; NEWMAN, T. J.: Emergent cell and tissue dynamics from subcellular modeling of active biomechanical processes. In: *Phys Biol* 8 (2011), Aug, Nr. 4, S. 045007
- [VK92] VAN KAMPEN, N. G.: *Stochastic Processes in Physics and Chemistry, Volume 1, Second Edition (North-Holland Personal Library)*. 2. North Holland, 1992 <http://www.worldcat.org/isbn/0444893490>. – ISBN 0444893490
- [WSJL07] WOLPERT, Lewis ; SMITH, Jim ; JESSELL, Tom ; LAWRENCE, Peter: *Principles of Development*. Third. Oxford University Press, 2007

Acknowledgment

First of all I want to thank my supervisor and advisor Ivo Sbalzarini for his steady support and the friendly atmosphere he created in the MOSAIC group. Thanks also to Frank Jülicher who agreed to be my first reviewer.

A special thank you goes to Paul Müller and Friedrich Anders for reviewing my manuscript.

Furthermore I thank Paul Göschel for the pleasant accommodation and giving this thesis a personal meaning and Johanna Zeil for her loving company through all ups and downs during that time. I want to thank my parents for their personal and financial support, Franziska Peter for her encouragement and Jonas Wick, Florian Kunert, Hanne Delling, Ulrike and Bernhard Feistel, Martin Hartwig and Bokonon for their inspiration.

Selbständigkeitserklärung

Gemäß §21 (8) der Diplomprüfungsordnung versichere ich, diese Diplomarbeit selbstständig verfasst und keine anderen Hilfsmittel und Quellen als die angegebenen verwendet zu haben. Leistungen anderer sind als solche ausgegeben.

Christian Bläsche

Dresden, February 2014